International Journal of Rock Mechanics & Mining Sciences 147 (2021) 104872

Contents lists available at ScienceDirect

International Journal of Rock Mechanics and Mining Sciences

journal homepage: www.elsevier.com/locate/ijrmms

The use of supercritical CO_2 in deep geothermal reservoirs as a working fluid: Insights from coupled THMC modeling

Quan Gan [a,b,*], Thibault Candela [d], Brecht Wassing [d], Laura Wasch [d], Jun Liu [e], Derek Elsworth [c]

[a] College of Resources and Safety Engineering, Chongqing University, Chongqing, China
[b] School of Geosciences, University of Aberdeen, UK
[c] Department of Energy and Mineral Engineering, EMS Energy Institute and G3 Center, Pennsylvania State University, University Park, PA, USA
[d] TNO, Utrecht, the Netherlands
[e] Institute of New Energy and Low-Carbon Technology, Sichuan University, Chengdu, 610065, China

ARTICLE INFO

Keywords:
THMC Coupling
Geothermal
Supercritical CO2
Permeability evolution

ABSTRACT

A coupled THMC (thermal-hydrological-mechanical-chemical) model is developed and applied to explore the potential feasibility of using $scCO_2$ (supercritical carbon dioxide) as a working fluid in geothermal reservoirs. This is achieved by examining the evolution of the kinetics of mineral precipitation-dissolution and its associated impact on the evolution of the rock permeability and porosity. The pH of the reservoir rapidly reduces from 7 to ~4.5–5 due to the fast dissolution of calcite. Chemical reactions and mineral dissolution and precipitation near the injector are suppressed by the plug-flow penetration of anhydrous $scCO_2$ displacing the original pore fluid. A conceptual three-zone model is proposed to illustrate the kinetic process of feldspar dissolution and precipitation depending on timing. The initial high concentration of K^+ prompts feldspar to precipitate in the first stage by consuming K^+ until 1*y*, Feldspar were dissolved into precipitations of illite, smectite, and siderite at 1-6*y*, with albite, muscovite and kaolinite mostly precipitated in the last stage 6–10*y*. The precipitations of secondary clay minerals and quartz serve to maintain the integrity of caprock sealing. Continuous $scCO_2$ injection under fully coupled THMC model shows a 1.4-times enhancement of fracture permeability and 1.2-times enhancement of matrix permeability dominated by chemical dissolution and thermal unloading process. The pronounced thermal drawdown is the principal factor in enhancing permeability and porosity near injection well. Furthermore, the expansive capability of CO_2 provides extra benefits in enhancing formation pressure to ensure consistent high flow rates, while achieving a higher thermal energy extraction efficiency and preventing scaling issues in wellbore. The mass concentration of scCO2 in the production well increased to 0.82 after $1.2 \times 10^8 s$ also leads to the enhancement of fluid enthalpy up to 6.5×10^5 J/kg, due to the high heat capacity of $scCO_2$. The injected CO_2 are sequestered at $\sim 2 \times 10^7$ kg at $t = 2 \times 10^8 s$ (6.34*y*) as the solubility trapping mechanism.

1. Introduction

The injection of supercritical CO_2 ($scCO_2$) has been suggested as an effective method to stimulate unconventional low permeability (tight) formations[1,2] and to recover coalbed methane (CBM) through competitive sorption.[3,4] Scoping calculations for application to enhanced geothermal systems (EGS) have also suggested the feasibility of utilizing $scCO_2$ as a superior working fluid to water.[5–7] Compared to conventional water-based hydrothermal systems, $scCO_2$ injection provides unique benefits in promoting buoyant convection and thereby potentially reducing parasitic power consumption - due to the favorable properties of lower viscosity and higher compressibility.[5,8] Although $scCO_2$ has a lower heat capacity than water, the enhanced flow rate potentially compensates through increased circulation rates. Furthermore, fugitive losses of $scCO_2$ to the formation will sequester CO_2 in different forms, i.e. by structural,[910] mineral,[11] residual and solubility trapping.[12]

The target formation will evolve into three steady-state zones defined by the state of the resident fluid mixtures (Fig. 1).[13] The native interstitial brine is displaced by $scCO_2$ at the injection well and a high CO_2 concentration plume develops (zone 1) near that wellbore. The absence of water potentially hinders dissolution of reactive minerals as CO_2 on its own is not a strong ionic solvent.[14] A mixture of water with dissolved CO_2 and $scCO_2$ as two distinct phases develops beyond the injection zone (zone 2) – due to a pH decrease upon dissolution of CO_2,

* Corresponding author. College of Resources and Safety Engineering, Chongqing University, Chongqing, China.
E-mail address: quan.gan@cqu.edu.cn (Q. Gan).

https://doi.org/10.1016/j.ijrmms.2021.104872
Received 23 February 2021; Received in revised form 7 June 2021; Accepted 20 August 2021

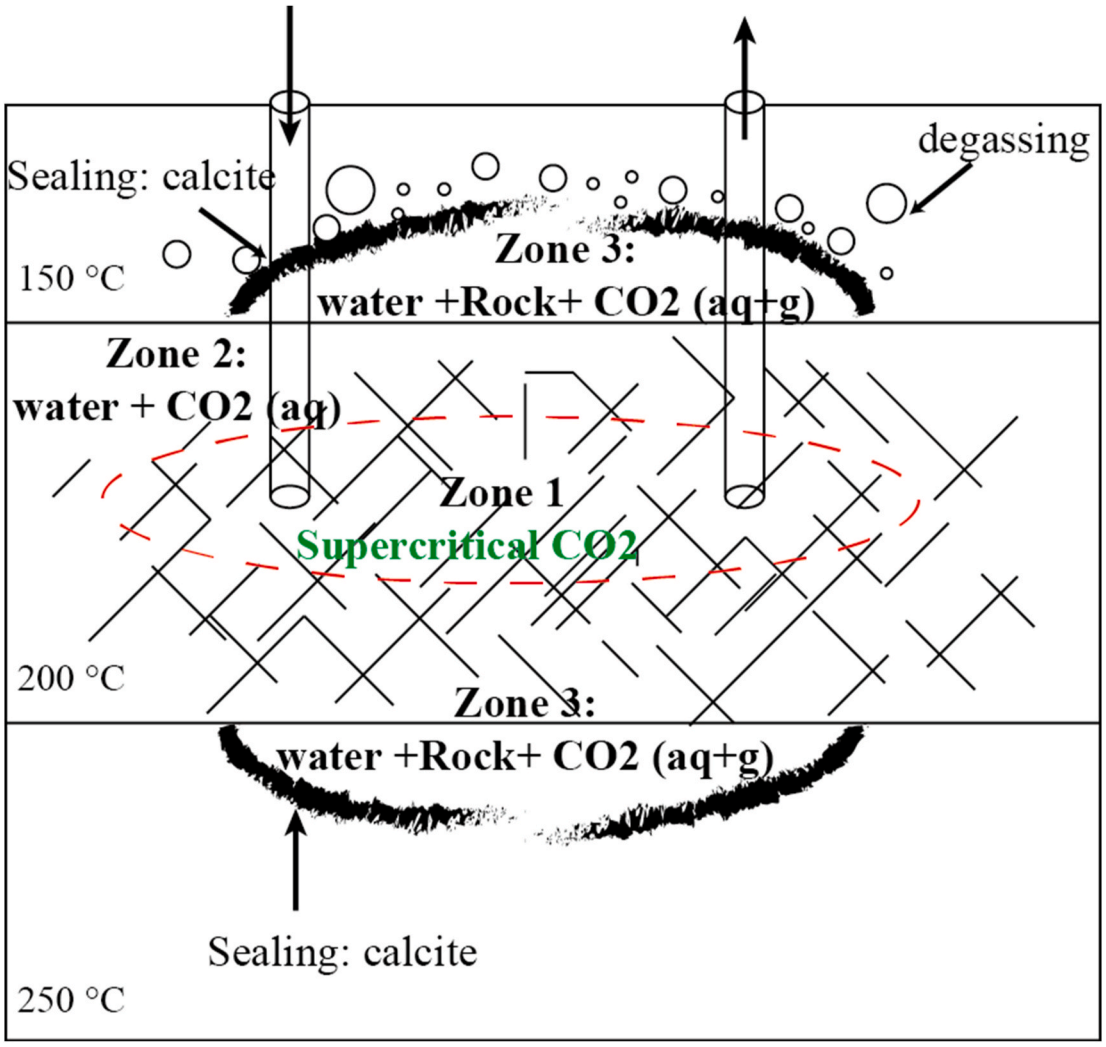

Fig. 1. Schematic of the evolution of a triple zoned reservoir following injection of $scCO_2$ into an EGS reservoir (modified after Ref.[13]).

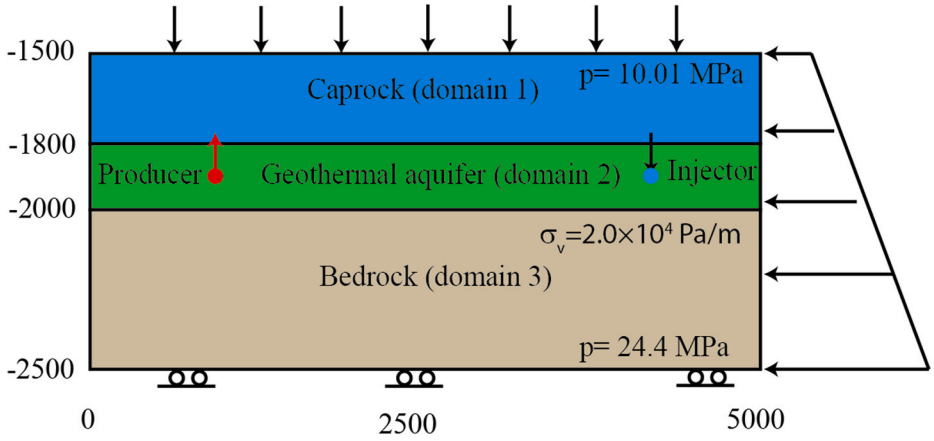

Fig. 2. Geometry and dimensions of conceptual model through the vertical section of interest showing the three distinct domains.

this zone experiences more rapid mineral dissolution, especially of calcite. Exterior to these two zones a cap-rock and bed-rock forms with a single aqueous phase and where calcite precipitates to seal the exterior of the reservoir.[15]

Circulating $scCO_2$ in geothermal formations poses significant challenges due to the inadequate understanding of the coupled thermal-hydro-mechanical-chemical process and feedbacks within the fractured medium. Temperature changes from thermal drawdown not only exert an impact in gaping or sealing fractures through induced thermal stress[16–18] but also impact mineral dissolution and precipitation rates with elevated pressure and temperature.[19] The subsequent induced chemical strain exerts a direct impact in modifying fracture aperture and

Table 1
Material properties for simulation and for the three domains comprising the model.[46]

Parameters	Caprock	Aquifer	Bedrock
Initial matrix permeability, m^2	10^{-17}	10^{-13}	10^{-17}
Initial fracture permeability, m^2	10^{-17}	10^{-13}	10^{-17}
Bulk modulus, GPa	15	15	15
Residua porosity	0.008	0.07	0.008
Maximum porosity	0.015	0.1	0.015
Initial porosity	0.014	0.085	0.014
Poisson's ratio	0.28	0.28	0.28
Rock density, kg/m^3	2600	2600	2600
Dilation angle, degrees	0	4	0
Non-linear stiffness, η	0.218	0.218	0.218
Residual aperture, m	1.78×10^{-5}	1.05×10^{-4}	1.81×10^{-5}
Maximum aperture, m	8.92×10^{-5}	5.26×10^{-4}	9.06×10^{-5}
Fracture spacing, m	50	1	50
Corey's irreducible water saturation, S_{lr}	0.2	0.2	0.2
Corey's irreducible gas saturation, S_{lr}	0.01	0.01	0.01
Leverett's function pressure, P_0 (Pa) (at zero stress)	1.0×10^8	1.0×10^8	1.0×10^8
Leverett's function, irreducible water saturation, S_{lr}	0.2	0.2	0.2

Table 2
Initial composition and volume fractions of primary and secondary minerals for the reactive transport simulations in TOUGH-ECO2N.[46]

Mineral	Chemical compositions	Volume fraction	Reactive surface area (cm^2/g)
Primary mineral			
Calcite	CaCO3	0.03	9.8
Quartz	SiO2	0.475	9.8
Oligoclase	$CaNa_4Al_6Si_{14}O_{40}$	0.28	9.8
K-feldspar	$KAlSi_3O_8$	0.2	9.8
Annite	$KFe_3AlSi_3O_{10}(OH)_2$	0.0075	9.8
Muscovite	$KAl_3Si_3O_{10}(OH)_2$	0.0075	151.6
Secondary mineral			
Kaolinite	$Al_2Si_2O_5(OH)_4$	0.0	151.6
Smectite-Na	$Na_{0.29}Mg_{0.26}Al_{1.77}Si_{3.97}O_{10}(OH)_2$	0.0	151.6
Chlorite	$Mg_{2.5}Fe_{2.5}Al_2Si_3O_{10}(OH)_8$	0.0	151.6
Illite	$K_{0.6}Mg_{0.25}Al_{1.8}(Al_{0.5}Si_{3.5}O_{10})(OH)_2$	0.0	151.6
Hematite	Fe_2O_3	0.0	12.9
Smectite-Ca	$Ca_{0.145}Mg_{0.26}Al_{1.77}Si_{3.97}O_{10}(OH)_2$	0.0	151.6
Albite	$NaAlSi_3O_8$	0.0	9.8
Dolomite	$CaMg(CO_3)_2$	0.0	9.8
Siderite	$FeCO_3$	0.0	9.8

Table 3
Initial total concentrations for primary chemical species.

Chemical species	Initial concentration (mol/kg)
H^+	0.0432
Na^+	0.99
K^+	5.98×10^{-3}
Ca^{2+}	4.737×10^{-3}
Mg^{2+}	2.669×10^{-5}
$HCO3^-$	4.562×10^{-2}
Cl^-	1.001
SiO_2(aq)	1.034×10^{-3}
Fe^{2+}	3.02×10^{-7}
SO_4^{2-}	1.32×10^{-9}
$AlO2^-$	1.361×10^{-8}

porosity[20–22] particularly through precipitation of kaolinite and feldspar.[23,24] Mechanical deformation is not only linked to the pore pressure changes driven by the injection of fluids and permeability evolution,[25–27] but also interconnected with chemical-mechanical creep processes through the destruction and rearrangement of asperity contacts in pressure solution together with fault healing.[28–30] Correspondingly, these complex interactions and feedbacks exert a strong control on the evolution of formation permeability and porosity requiring representation by a complex coupled THMC model.

This work presents a new THMC model by coupling $FLAC^{3D}$ with the TOUGH-ECO2N code,[31] enabling the simulation of reactivate transport of $scCO_2$ within fractured reservoirs and under non-isothermal and multiphase conditions. The embedded constitutive models combine the complex behaviors of fracture shear dilation-compaction, chemical-mechanical creep, mineral reaction (dissolution-precipitation) and resulting pore space clogging or erosion and their impacts on permeability. A contact-area-based mechanism allows the direct measurement of mineral infilling volume fraction change across the fracture surface due to fracture deformation.[28] To assess the influence of each individual component in the T-H-M-C quadruplet in changing permeability and porosity within the fracture and matrix, five scenarios of fully-coupled or partly-decoupled models are developed to examine the spatial profile for an orthogonal set of fractures. Fracture infill volume fraction changes for each mineral phase are utilized to detail the kinetic process of dissolution and precipitation over the projected 10 years of operation. The influence of geochemical reactions between $scCO_2$ and constituent minerals and associated thermal energy extraction are explored by contrasting the performance of both $scCO_2$ and water as the working fluids. We use this approach to gain a physics-based understanding of THMC interactions and impacts on performance.

2. Methodology and constitutive models

The proposed fully coupled thermal-hydro-mechanical-chemical model initiates from the original single phase (water/brine) non-isothermal EOS1 module and coupling structure.[32] This has been upgraded to accommodate the coupling of TOUGH-ECO2N with $FLAC^{3D}$. This enables the analysis of non-isothermal multiple-phase reactive transport with elastic-plastic deformation. We detail the principal features of the revised model in accommodating the governing equations and constitutive models for porosity and permeability evolution.

2.1. Conservation of fluid mass and energy (thermal + hydraulic)

Fluid flow and reactive transport modules are executed in the TOUGH-ECO2N model accommodating Darcy flow. Conservation of mass and energy are maintained in a series of iterations for fluid, aqueous species and energy based on the governing equation in the integral form,

$$\frac{d}{dt}\int_V M_k dV = \int_\Gamma F_k \cdot n + \int_V q_k dV \tag{1}$$

where the left hand term M_k represents the rate of the accumulated quantity, including flux, mineral mass, and thermal energy over each time step dt, stemming from the inward fluxes/energy F_k across the boundary Γ and the original volume/quantity in the volume dV. q_k represents sink or source of fluid, aqueous species, and thermal energy. The subscript k represents each component (water, gas, mineral species, aqueous species etc.). Equation (1) may be transformed into a PDE based on the divergence theorem,

$$\frac{dM_k}{dt} = -\nabla \cdot F_k + q_k \tag{2}$$

where q_k is the heat/flux sink from the injection or production well.

Table 4
Kinetic parameters for mineral dissolution and precipitation.[47]

Mineral	Parameters for kinetic rate law							
	Neutral mechanism		Acid mechanism			Base mechanism		
	k_{25}(mol/m^2/s)	E_a(kJ/mol)	k_{25}	E_a	n(H^+)	k_{25}	E_a	n(OH^-)
Primary								
Calcite	1.55×10^{-9}	23.5	1.55×10^{-6}	14.4	1			
Quartz	1.02×10^{-14}	87.7						
Oligoclase	1.445×10^{-13}	69.80	2.13×10^{-11}	65	0.457			
K-feldspar	3.89×10^{-13}	38	8.71×10^{-11}	51.7	0.5	6.31×10^{-22}	94.1	−0.82
Annite	2.82×10^{-13}	22	1.45×10^{-10}	22	0.525			
Muscovite	2.818×10^{-14}	22	1.41×10^{-12}	22	0.37	2.82×10^{-15}	22	−0.22
Secondary								
Kaolinite	6.918×10^{-14}	22.2	4.898×10^{-12}	65.9	0.777	8.91×10^{-18}	17.9	−0.47
Smectite-Na	1.66×10^{-13}	35	1.047×10^{-11}	23.6	0.34	2.02×10^{-17}	58.9	−0.4
Chlorite	2.02×10^{-13}	88	7.762×10^{-12}	88	0.5			
Illite	1.66×10^{-13}	35	1.05×10^{-11}	23.6	0.34	3.02×10^{-17}	58.9	−0.4
Hematite	2.51×10^{-15}	66.2	4.07×10^{-10}	23.6	0.34			
Smectite-Ca	1.66×10^{-13}	35	1.047×10^{-11}	23.6	0.34	2.02×10^{-17}	58.9	−0.4
Albite	2.75×10^{-13}	69.8	6.92×10^{-11}	65	0.457	2.51×10^{-16}	71.0	−0.57
Dolomite	2.95×10^{-8}	52.2	6.46×10^{-4}	36.1	0.5			
Siderite	1.26×10^{-9}	62.8	6.46×10^{-4}	36.1	0.5			

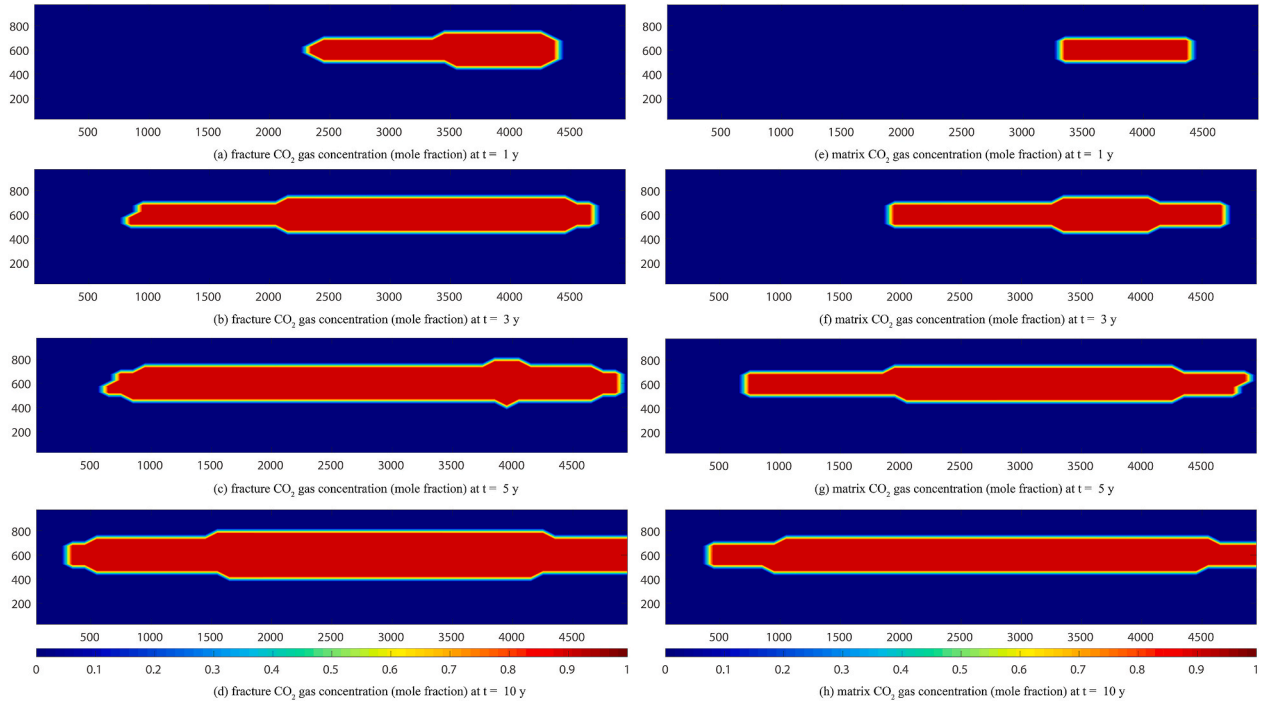

Fig. 3. Evolution of CO_2 gas concentration (mole fraction) in fractures (left side) and matrix (right side) from 1 to 10*y*.

2.2. Conservation of momentum

Mechanical equilibrium for the system is governed by momentum balance as

$$\sigma_{ij,j} + f_i = \rho \frac{dv_i}{dt} \tag{3}$$

where $\sigma_{ij,j}$ is the divergence of the transposed Cauchy stress tensor, f_i is the body force and v_i is the velocity of the solid particles. Hence, the expression may be simplified when the solid is at equilibrium, as,

$$\sigma_{ij,j} + f_i = 0 \tag{4}$$

Considering the induced thermal expansion resulting from transfer of heat energy, and poroelastic response of a single/dual-porosity medium, a new stress-strain constitutive relationship registers the response of the dual-porosity medium (1 for fracture, 2 for matrix) as,[33]

$$\sigma_{ij} = 2G\varepsilon_{ij} + \frac{2Gv}{1-2v}\varepsilon_{kk}\delta_{ij} - \left(\alpha_p^1 p + \alpha_p^2 p\right)\delta_{ij} - \alpha_T T\delta_{ij} \tag{5}$$

where G is the shear modulus, v is the Poisson ratio, α_p is the Biot coefficient, p is fluid pressure, T is rock temperature and α_T is the thermal expansion coefficient. The stress-strain relation is defined as,

$$\varepsilon_{ij} = \frac{1}{2}\left(u_{i,j} + u_{j,i}\right) \tag{6}$$

Combining equations (4)–(6) yields an expression representing stresses and displacements in equilibrium as the Navier equation,

$$G\nabla u_{i,kk} + \frac{G}{1-2v}u_{k,ki} - \left(\alpha_p^1 p + \alpha_p^2 p\right)_{,i} - \alpha_T T_{,i} + f_i = 0 \tag{7}$$

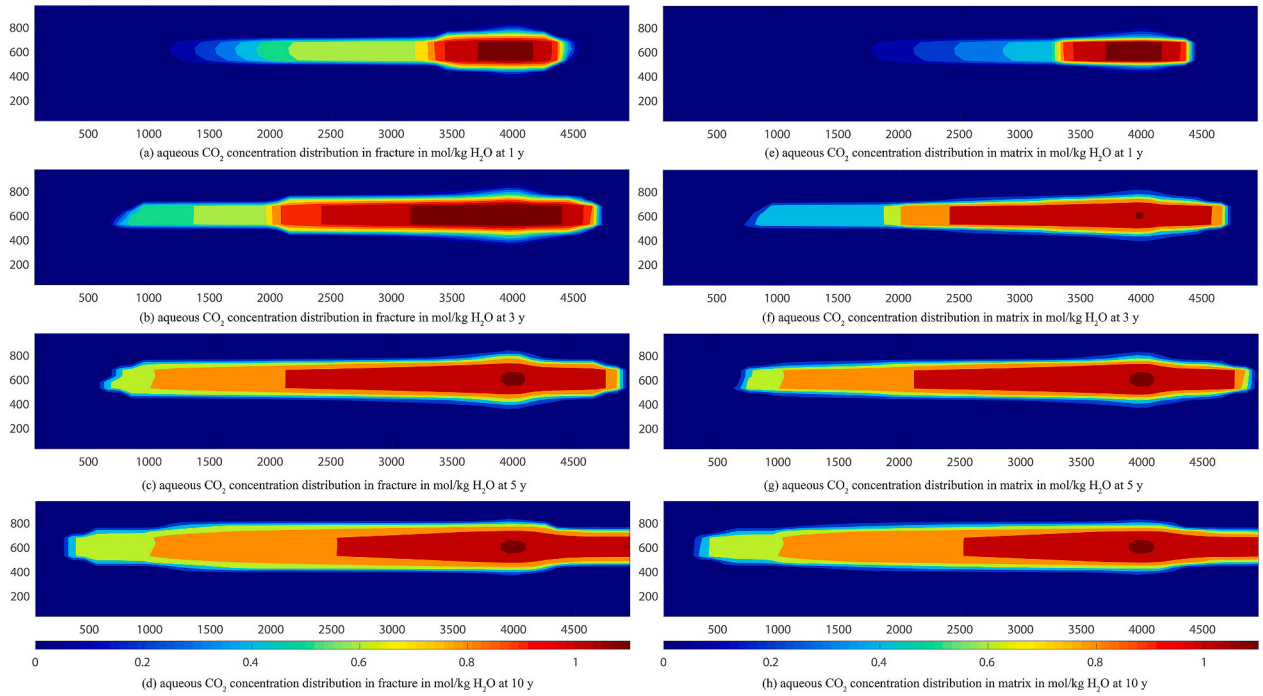

Fig. 4. Evolution of aqueous CO_2 concentration (mole per kg) in fractures (left side) and matrix (right side) from 1 to 10*y*.

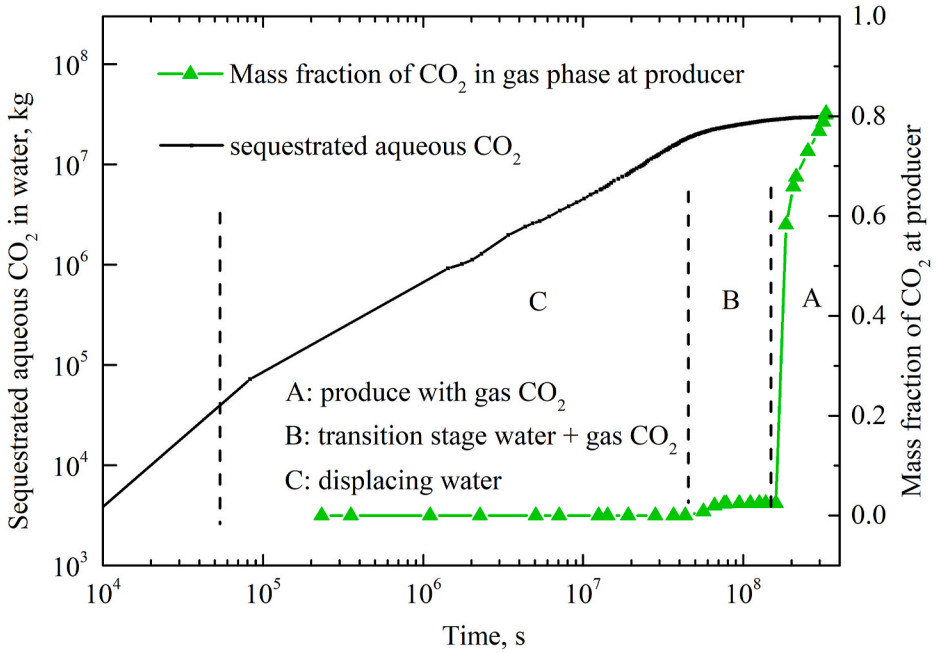

Fig. 5. Sequestrated mass of aqueous CO_2 over 10*y* (black), and associated mass fraction of CO_2 at producing well (green). (For interpretation of the references to colour in this figure legend, the reader is referred to the Web version of this article.)

2.3. Reactive transport, dissolution & precipitation

The governing equation for reactive solute transport is based on a molar balance for each mineral component. The aqueous chemical reactions are assumed to be at local equilibrium. This is represented by a similar expression to that for general mass conservation (equation (2)). The mass accumulation term M_k will be replaced by the molar concentration of individual species as,

$$M_k = \varphi S_l \rho_l X_l^k + \varphi S_g \rho_g X_g + (1-\varphi)\rho_s X_s \quad (8)$$

where φ is the porosity, ρ is the density of the fluid, gas, or solid, S is the saturation of each phase and X_l^k is the total mass fraction of primary component or chemical species k in the liquid phase. The third term for the solid phase will be removed when calculating the fluid mass accumulations. Therefore, the flux term F in the original equation (2) representing the advection-diffusion process is simplified as,

$$F = \sum_{\beta=l,g}\left(-X_\beta \rho_\beta \frac{K k_\beta^r}{\mu_\beta}\left(\nabla p_\beta - \rho_\beta g\right)\right) - \lambda_\beta \nabla C \quad (9)$$

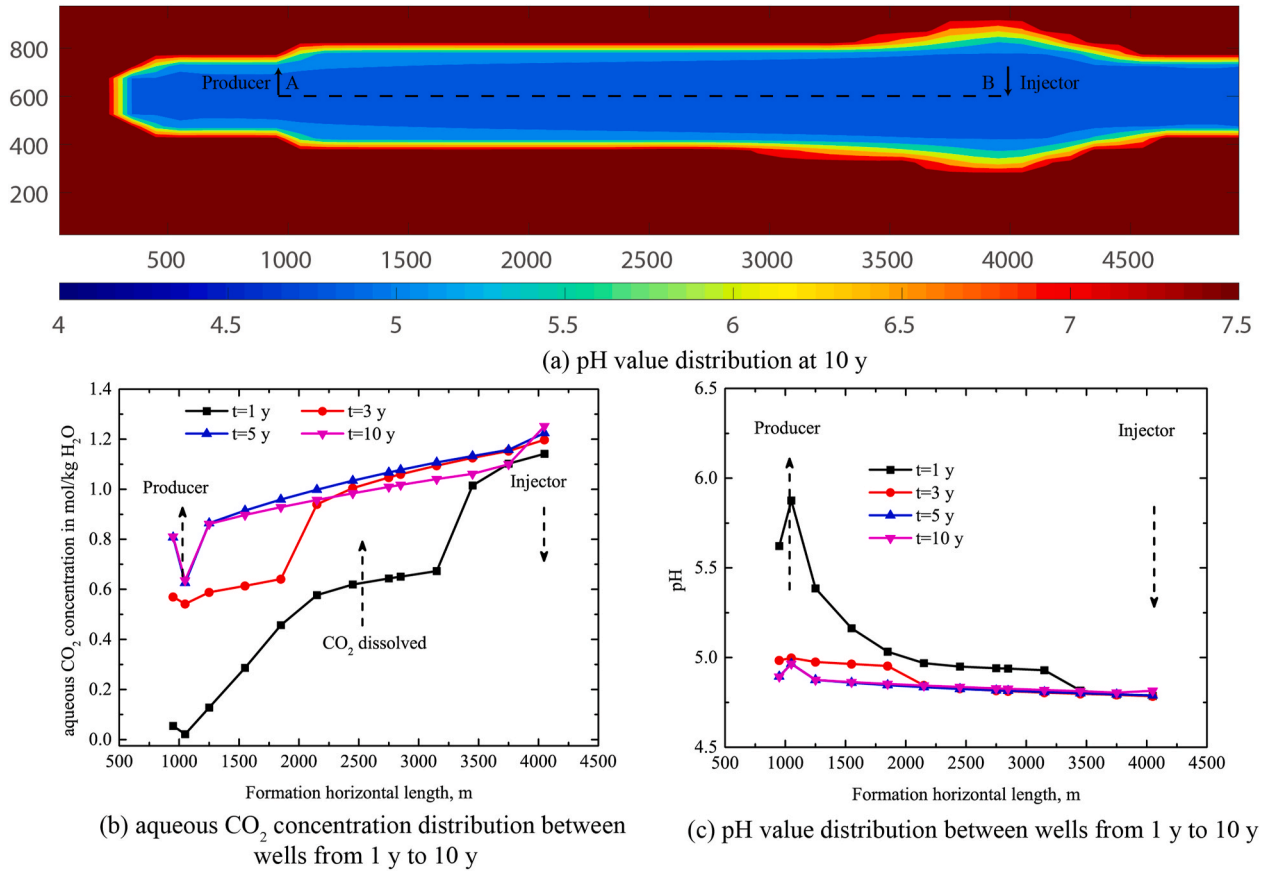

Fig. 6. Distribution of (a) pH after 10 y and the associated (b) evolution of aqueous CO_2 concentration, and (c) pH distribution with elapsed time 1–10*y*.

where the first term quantifies advection based on the concept of Darcy's law for multiphase flow with a relative permeability k_β^r, where K is the absolute permeability, μ_β is the dynamic viscosity of phase β and X_β is the total mass fraction for each phase (liquid or gas). The second term represents diffusive transport for solutes (Fickian) or heat (Fourier) driven by concentration or thermal gradients. Hence, the parameter λ_β represents the chemical diffusion coefficient or thermal conductivity, and ∇C is the gradient of concentration or temperature. In this work, the chemical flux λ_β is calculated as $\lambda_\beta = \rho_\beta \tau \varphi S_\beta D_\beta$, where τ is tortuosity and D_β is the diffusion coefficient.

The TOUGH-ECO2N module defines primary species and secondary aqueous complexes with the assumption of instantaneous local equilibrium. This assumption of local equilibrium significantly reduces the number of chemical unknows in the equations, while maintaining the accuracy of the reaction rate in a given chemical condition. The total concentration C_j for the primary species j can be expressed as,

$$C_j = c_j + \sum_{k=1}^{N_x} v_{kj} C_k + \sum_{m=1}^{N_p} v_{mj} C_m + \sum_{n=1}^{N_q} v_{nj} r_n \Delta t \tag{10}$$

where c_j is the individual concentration for the *j-th* species, j and k are the indices of the primary species and secondary complex, m is the mineral under the equilibrium condition, and n is the mineral under kinetic constraints. N_x is the total number of aqueous secondary chemical species, N_p is the total number of reactions between solid mineral and aqueous species under equilibrium, and N_q is the number of reactions between solid mineral and aqueous species. v_{kj}, v_{mj}, v_{nj} are stoichiometric coefficients of the primary species in the aqueous complexes, equilibrium and kinetic minerals. The concentration of the *k-th* aqueous complexes (secondary) c_k may be quantified as a function of concentrations of primary species j as,

$$c_k = K_k^{-1} \gamma_k^{-1} \prod_{j=1}^{N_c} c_j^{v_{kj}} \gamma_j^{v_{kj}} \tag{11}$$

where c_j is the molar concentration of the *j-th* species, K_k is the equilibrium constant of the *k-th* secondary species complexation reaction, γ_k and γ_j are the thermodynamic activity coefficients of the *k-th* secondary and *j-th* primary species. r_n is the kinetic rate as a function of the concentrations of the primary chemical species which governs the response of dissolution and precipitation kinetics. A generalized law is provided for predicting dissolution/precipitation of the *n-th* mineral[34] as,

$$r_n = -\operatorname{sgn}\left[\log\left(\frac{Q_n}{K_n}\right)\right] k_n A_n \left|\left[\left(\frac{Q_n}{K_n}\right)^{\mu} - 1\right]\right|^{\eta} \tag{12}$$

where r_n is the dissolution/precipitation rate. A positive value indicates dissolution, and a negative value precipitation. k_n is the rate constant for the *n-th* mineral reaction with water in transforming 1 mol of mineral, which is also a function of temperature. Q_n is an ion activity product. μ and η are the coefficients determined by experiments, usually assumed as 1. The rate constant k is expressed by an Arrhenius equation as,[34,35]

$$\begin{aligned} k = {} & k_{25}^{n} \exp\left[\frac{-E_a^n}{R}\left(\frac{1}{T} - \frac{1}{298.15}\right)\right] \\ & + k_{25}^{\mathrm{H^+}} \exp\left[\frac{-E_a^{\mathrm{H^+}}}{R}\left(\frac{1}{T} - \frac{1}{298.15}\right)\right] a_{\mathrm{H^+}}^{n_{\mathrm{H^+}}} \\ & + k_{25}^{\mathrm{OH^-}} \exp\left[\frac{-E_a^{\mathrm{OH^-}}}{R}\left(\frac{1}{T} - \frac{1}{298.15}\right)\right] a_{\mathrm{OH^-}}^{n_{\mathrm{OH^-}}} \end{aligned} \tag{13}$$

where k_{25} is the rate constant at 25 °C, E_a is the activation energy, R is the gas constant, T is absolute temperature, $a_{\mathrm{H^+}}^{n_{\mathrm{H^+}}}$ is the activity of H^+,

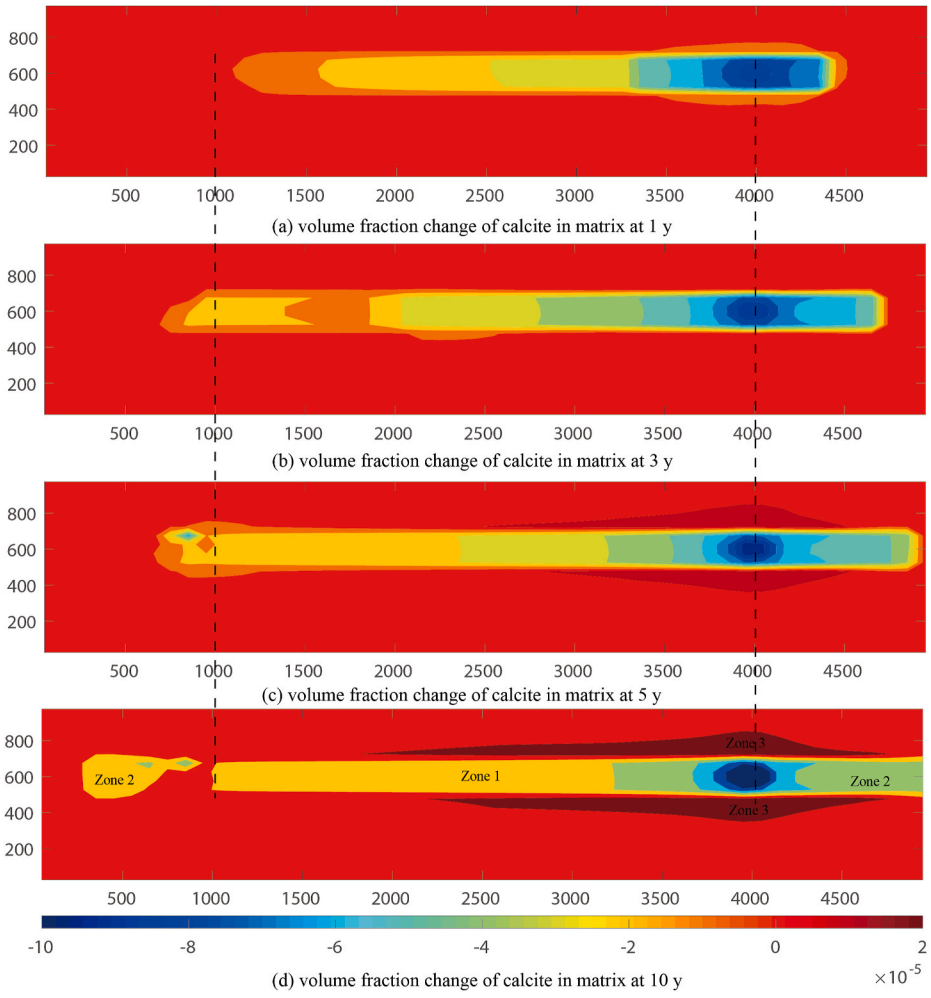

Fig. 7. Evolution of volume fraction change of calcite in fracture (left side) and matrix (right side) from 1 to 10*y*.

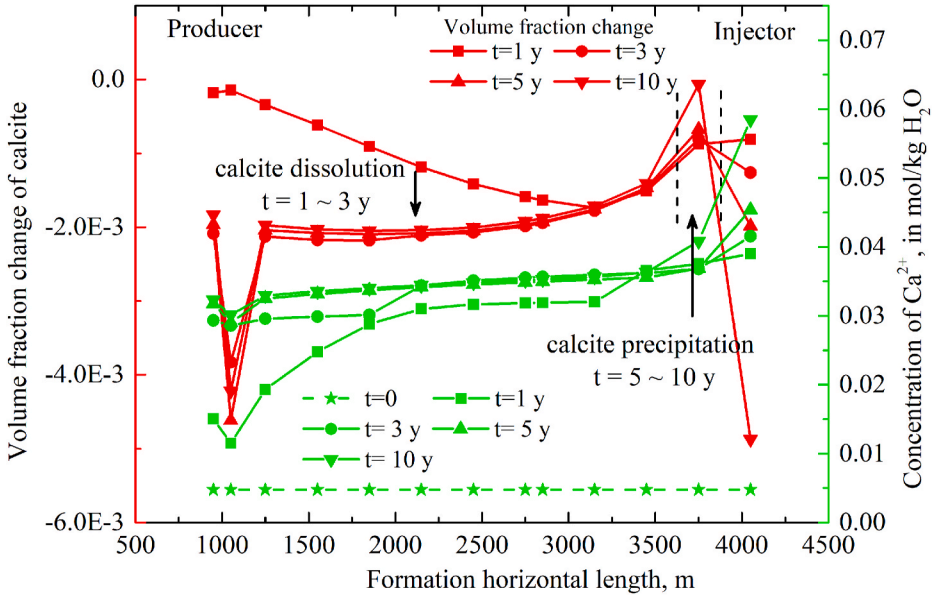

Fig. 8. Change in distribution of volume fraction of calcite (red) from injector to producer, and the spatial distribution of Ca^{2+} concentration (green) from 1 to 10 *y*. (For interpretation of the references to colour in this figure legend, the reader is referred to the Web version of this article.)

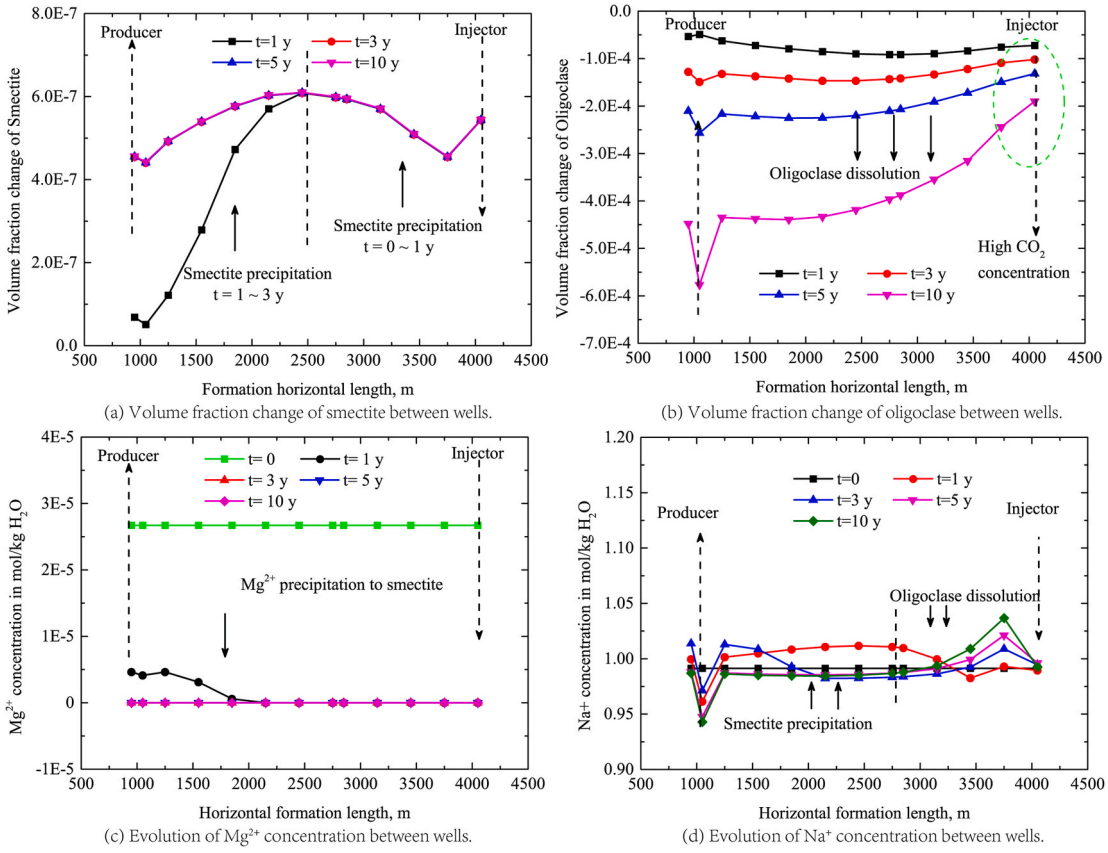

Fig. 9. Evolution of volume fraction change of (a) smectite, (b) oligoclase, (c) Mg^{2+}, and (d) Na^{+} concentrations between injector and producer from 0 to 10 *y*.

defined as the product of concentration of H^+ (c_{H^+}) and activity coefficient γ_{H^+}. $a_{OH^-}^{n_{OH^-}}$ is the activity of OH^-, defined by the product of concentration of OH^- (c_{OH^-}) and activity coefficient γ_{OH^-}. In describing the process of dissolution-precipitation, the above equations contain three mechanisms which are not limited to only pure H_2O as a neutral mechanism but also includes acid (H^+) and base mechanisms (OH^-).

2.4. Permeability and porosity evolution

Permeability and porosity in a dual-porosity medium (fracture and matrix) accommodate various constitutive mechanisms, including stress dependent evolution of permeability and porosity and mineral dissolution–precipitation. The fracture networks are defined using the MINC (Multiple Interacting Continua) approach in TOUGH-ECO2N, while specifying the three conjugate sets of fractures within the aquifer layer. We elaborate on details of these models in changing the properties of both media.

Porosity changes in response to both mechanical deformation and chemical reaction. The stress dependency follows,[36,37]

$$\varphi = \varphi_r + (\varphi_0 - \varphi_r)e^{-\alpha\tau'} \tag{14}$$

where φ_0 is the porosity at zero effective stress, φ_r is porosity conforming to high effective stress, τ' is effective mean stress and the exponent α is a constant parameter representing rock compressibility (1/Pa). The removal or deposition of mineral mass within the continuum elements results in a direct change in fracture or matrix porosity, which is mediated by the total volume fraction change[38] as,

$$\varphi_c = 1 - \sum_{m=1}^{N_m} f_m - f_u \tag{15}$$

where N_m is the total number of reactive minerals, f_m is the total mineral volume fraction ($V_{mineral}/V_{medium}$) for the *m-th* mineral, and f_u is the non-reactive mineral fraction. In the iterative modelling process, the contribution of porosity change due to dissolution/precipitation is quantified by obtaining the volume fraction change $\Delta\varphi_c$ relative to the initial total volume fraction of the mineral as,

$$\Delta\varphi_c = \varphi_c - V_{ini-m}/V_{medium} \tag{16}$$

$$\varphi_{total} = \varphi + \Delta\varphi_c \tag{17}$$

Changes in fracture and matrix permeability are treated as separate processes. The gaping or sealing of fracture aperture must accommodate processes of shear dilation, normal compaction closure, stress-enhanced pressure solution, and chemical precipitation. The hydro-mechanical response modifies the fracture aperture through the variation of effective normal stress as [Min et al., 2009],

$$b_s = b_r + (b_{max} - b_r)\exp\left(-\eta\left(\sigma' - \sigma_0'\right)\right) \tag{18}$$

where b_r represents the residual aperture (m), b_{max} is the maximum aperture at zero stress (m) and η is the non-linear fracture stiffness (1/MPa). The shear displacement of the fractures u_{js} provides a contribution in increasing normal aperture b_{dila} by dilation according to,

$$b_{dila} = u_p \tan\psi_d \tag{19}$$

where u_p is the plastic shear strain increment and ψ_d is the dilation angle. The fractures are initially filled with both reactive and non-reactive minerals. The magnitude of aperture changes b_{chem} due to dissolution – precipitation is quantified as,[28]

$$b_{chem} = b_{ini}\left[1 - \left(\frac{V_m^1}{V_T} + \frac{dV_m^R}{V_T}\right)\cdot\frac{f_\sigma}{V_c}\right], \quad f_\sigma = \left(1 - \frac{db_m}{b_{ini}}\right) \tag{20}$$

where b_{ini} is the initial aperture for the individual fracture in the

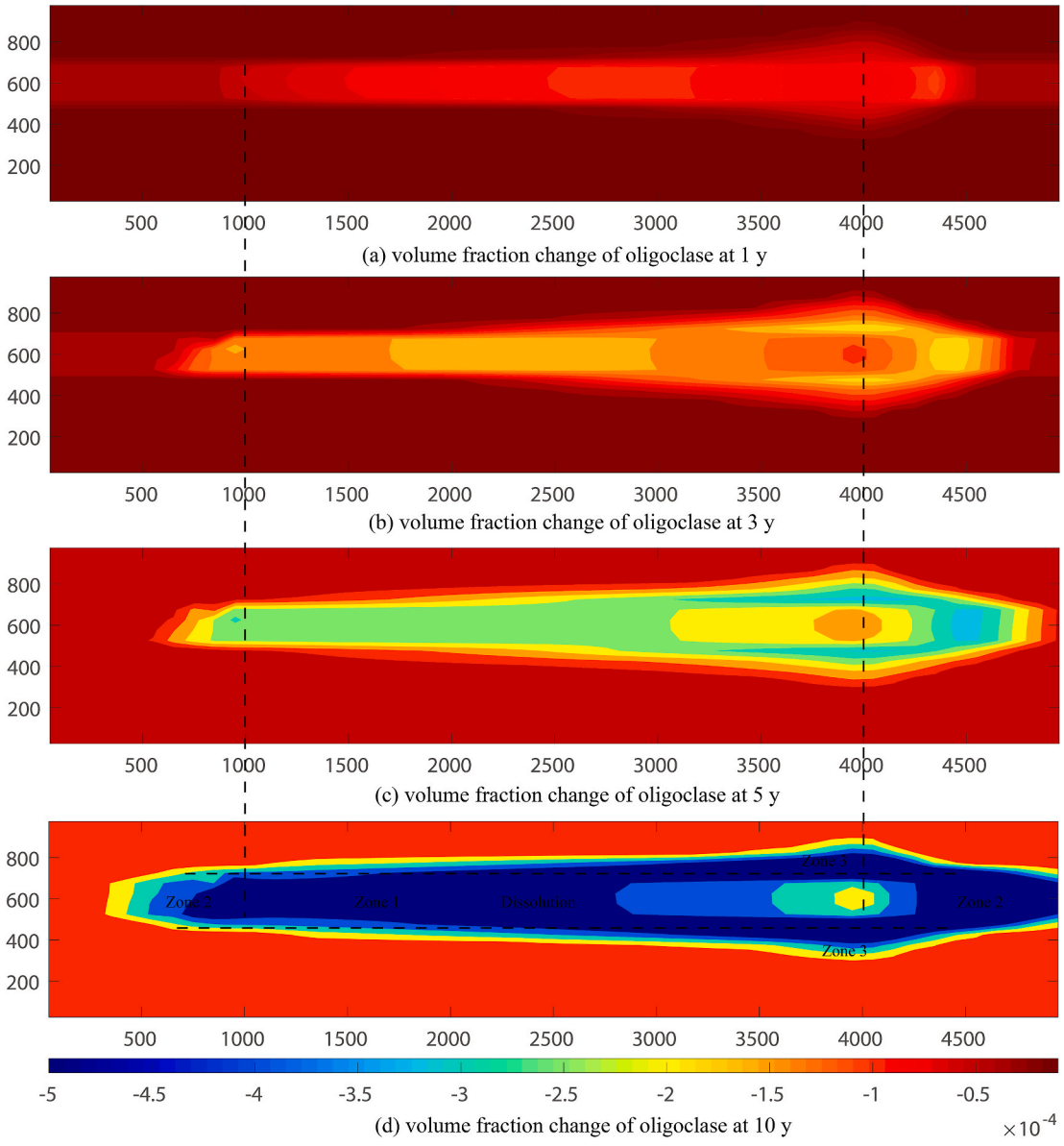

Fig. 10. Volume fraction change of oligoclase at (a) 1*y*, (b) 3*y*, (c) 5y, and (d) 10 *y*.

element, db_m is the change in fracture aperture due to mechanical factors defined as $db_m = (b_s + b_{dila} - b_{ini})/3$, V_c is the critical mineral volume fraction when the permeability reduces to 0. V_m^1 is the volume fraction change of the non-reactive minerals, while dV_m^R is the volume fraction change of reactive minerals due to dissolution or precipitation. Consequently, the composite aperture b_{total} may be determined by combining equations 18–20 as,

$$b_{total} = b_s + b_{dila} + b_{chem} \tag{21}$$

The final composite expression for calculating the permeability of fractures is given based on the cubic relation with aperture and fracture spacing s for a parallel-plate model[39] as,

$$k = \frac{b_{total}^3}{12s} \tag{22}$$

The matrix permeability k_{matrix} is correlated to the evolution of porosity by the classical Kozeny-Carman model[40] as the matrix porosity evolution is associated with the combined effects of mechanical deformation and geochemical reactions.

$$k_{matrix} = k_i \frac{(1-\varphi_{ini})^2}{(1-\varphi)^2} \tag{23}$$

3. Reservoir characteristics and model

A candidate geology for modelling $scCO_2$ injection is selected from the St. John's Dome on the border between Arizona and New Mexico. This site is relevant as large volumes of naturally-occurring CO_2 occupy the dome.[41] Our conceptual numerical model is of pseudo 2-D geometry in the vertical profile with dimensions of 5000 *m* (horizontal) × 10 *m* (horizontal) × 1000 *m* (vertical) (Fig. 2). The basal confining bed is 2500 *m* below the ground surface. Three different domains represent the caprock (300 *m* thick), target geothermal aquifer (200 *m* thick), and bottom bedrock (500 *m* thick), respectively. An injector and another production well are located at a depth of 1900 *m* and 1000 *m* from the right and left vertical boundaries, respectively. The $scCO_2$ injection schedule is at a constant rate of 1 kg/s at 35 °C for 10 years – this low rate is a limitation of the constrained CO_2 PVT properties defined in the TOUGH-ECO2N module. The hot fluids are collected at the outlet with

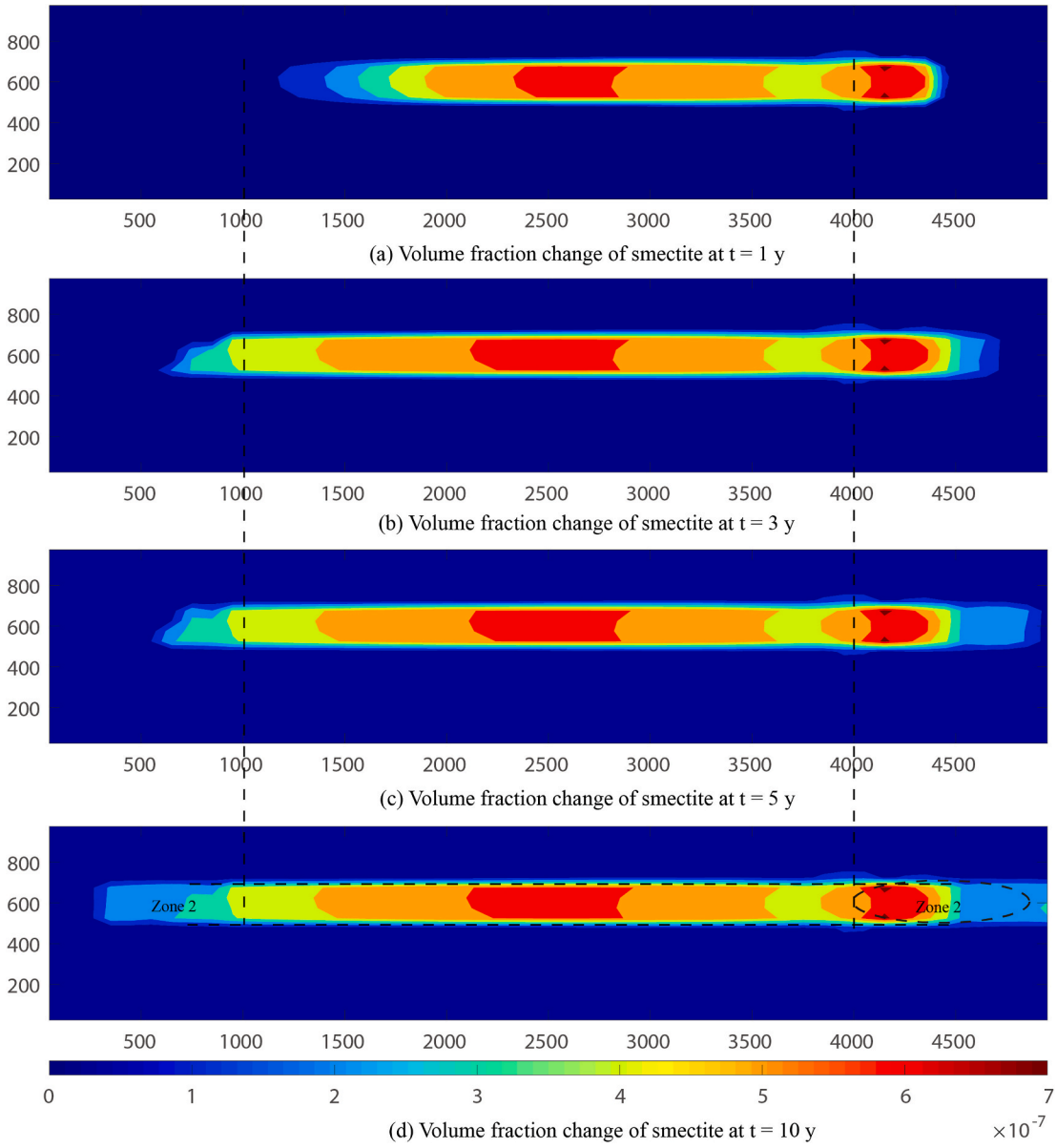

Fig. 11. Change in volume fraction of smectite at (a) 1*y*, (b) 3*y*, (c) 5y, and (d) 10*y*.

constant bottom hole pressure at 12 MPa.

The initial pore pressure distribution is hydrostatic at 9.8×10^3 Pa/*m* with a maximum bottom hole pressure of 19.46 MPa and an initial homogeneous formation temperature of 90 °C. The initial principal stress state in the underlying confining bed is 47.0 MPa, 53.5 MPa, and 60 MPa in the horizontal and vertical directions, with a horizontal stress gradient of 1.6×10^4 Pa/*m* and 1.8×10^4 Pa/*m* and a vertical stress gradient set to 2.0×10^4 Pa/*m*. The initial permeability and porosity of the overlaying and underlaying seals are isotropic and uniform at 10^{-17} m^2 and 0.014 with the initial stress applied while the initial permeability and porosity for the reservoir set to 10^{-13} m^2 and 0.085. The parameters for Corey's relative permeability model and Leverett's capillary pressure model[42,43] are provided in Table 1. The irreducible water saturation is 0.2 with an irreducible gas saturation is 0.01, allowing excess gaseous CO_2 to migrate as gas bubbles to the base of the overlaying caprock.[44] The relative permeability model is defined as,[45]

$$k_{rl} = S_{nl}^4$$
$$k_{rg} = (1 - S_{nl})^2\left(1 - S_{nl}^2\right) \quad (24)$$

where $S_{nl} = (S_l - S_{lr})/(1 - S_{lr} - S_{gr})$.

Table 2 defines the initial chemical composition and volume fraction of six primary and secondary minerals. Table 3 provides the initial concentrations of the primary aqueous species in the boundary water at equilibrium with the constituent minerals of the aquifer. The relevant kinetic parameters for all minerals are provided in Table 4 - as used in Equation (13) to quantify the dissolution/precipitation potential of each component.

4. Results and discussion

Given this prior background of the initial setting, continuous $scCO_2$ injection is anticipated to induce significant changes in the composition and distribution of minerals through reaction and dissolution–precipitation. This will modify the associated permeability and porosity via various THMC process interactions and feedbacks. We explore the spatial and temporal evolution of mineral distribution and its impact on permeability.

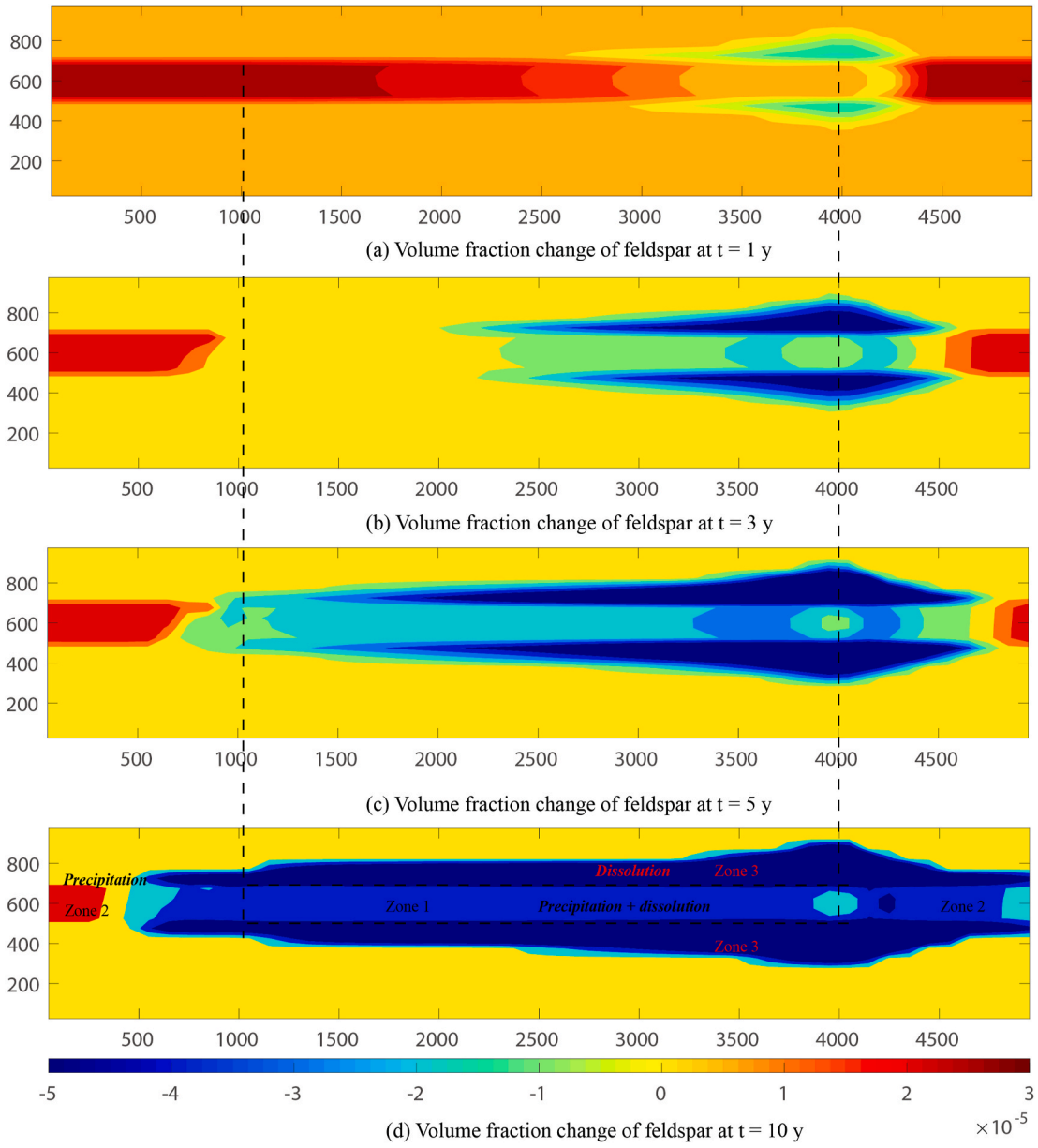

Fig. 12. Change in volume fraction of feldspar at (a) 1*y*, (b) 3*y*, (c) 5*y*, and (d) 10*y*.

4.1. CO_2 dissolution

As the initial porosity and permeability in the aquifer is significantly higher than that of the caprock and bedrock, the brine CO_2 mixture is transported primarily in the intervening reservoir. The CO_2 is in both gaseous and aqueous phases and is in equilibrium with the aqueous state as,

$$\begin{aligned} &CO_2(sc) \rightleftarrows CO2(aq) \\ &CO_2(aq) + H_20 \rightarrow HCOJ_3^- + H^+ \end{aligned} \tag{25}$$

where *sc* refers to the supercritical state, and *aq* denotes the aqueous phase. The above reaction indicates that the dissolution of CO_2 results in the acidification of the brine through the generation of carbonic acid as a form of solubility trapping. Fig. 3 shows the evolution of CO_2 gas concentration (mole fraction) from 1*y* to 10*y* in the fractures and matrix separately. It reveals that part of the gaseous CO_2 has penetrated and diffused into the caprock and bedrock near the injector starting from 1*y*, after the CO_2 plume has occupied the majority pore space in the reservoir. The diffusion velocity of gas CO_2 in the fracture is higher than the velocity travelling in the matrix. The CO_2 invades the caprock to a maximum height of 100 *m* after 10 years of injection (Fig. 3c). The accumulated aqueous phase CO_2 in the caprock and bedrock is simultaneously consumed by the dissolution/precipitation of secondary minerals. Fig. 4 shows the aqueous CO_2 distribution from 1*y* to 10*y*, confirming the expansion of the aqueous CO_2 plume migrating into the caprock and bedrock adjacent to the injector. The reduction of aqueous CO_2 concentration from 5*y* to 10*y* suggests the extraction of CO_2 from the production well, while the dissolution of CO_2 in the brine reached the peak magnitude.

Given the low permeability sealing from caprocks in the reservoir, the major form of CO_2 trapping is anticipated to be solubility trapping in the aqueous phase. The cumulative mass of aqueous CO_2 sequestered in water is described by the black line in Fig. 5. The abundance of CO_2 in the aqueous phase may be calculated as,

$$M_{CO_2}^l = \sum_{n=1}^{total} \left(V_n \varphi_n S_n^l \rho_l X_{CO_2} \right) \tag{26}$$

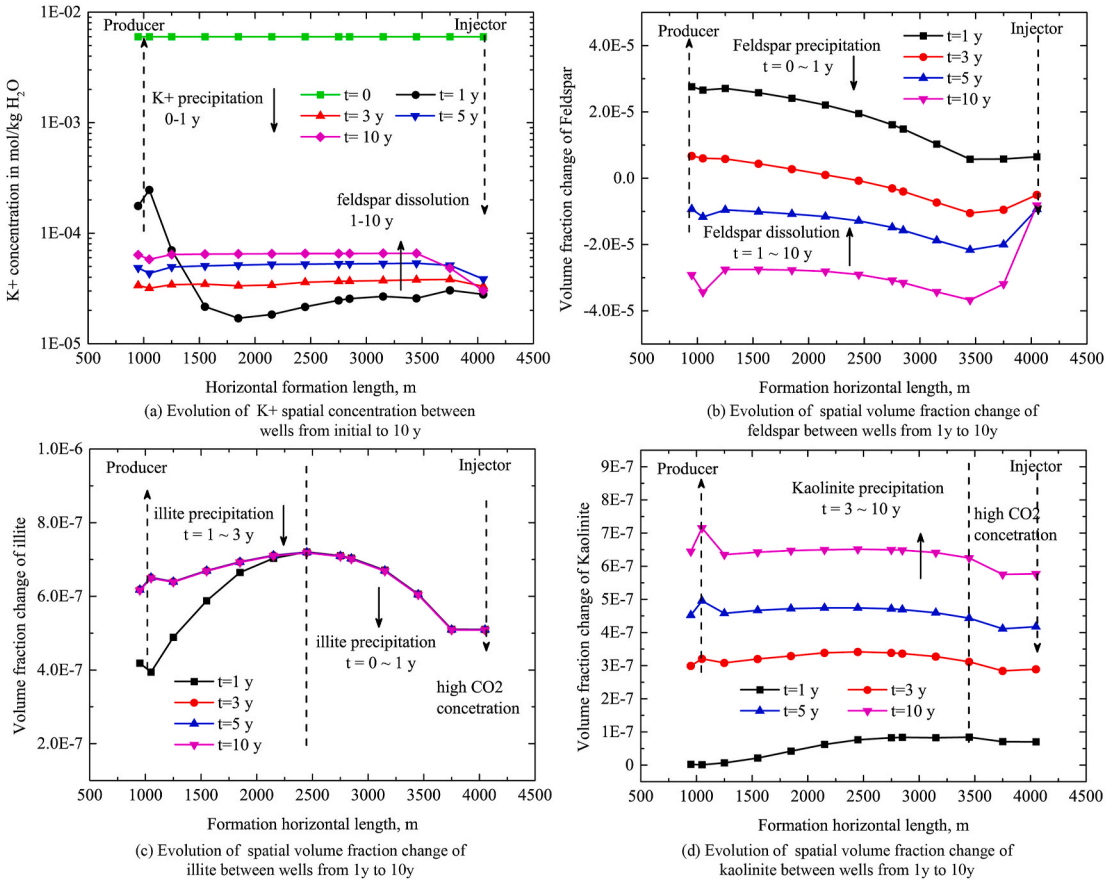

Fig. 13. Evolution of change in volume fraction of (a) K^+, (b) feldspar, (c) illite, and (d) kaolinite between the wells from 1*y* to 10*y*.

where n represents the number of the element solution block. V is the element volume, φ_n is porosity, S_n^l is the liquid saturation and X_{CO_2} is the mass fraction of CO_2 in the aqueous phase. The cumulative mass of dissolved CO_2 reaches the maximum capacity of $\sim 2 \times 10^7\ kg$ at $t = 2 \times 10^8 s$ (6.34*y*), increasing only slowly thereafter. Accordingly, the mass fraction of CO_2 abundance evolution in the outlet fluids also reaches a stable state at $t = 2 \times 10^8 s$ (6.34*y*). Continuous $scCO_2$ injection displaces the original pore fluid towards the producer as dehydration occurs. The dissolved $CO_2(aq)$ arrives at the producer from $t = 5 \times 10^7 s$ (1.6*y*), given the 3000 *m* travelling distance between the wells. The mass fraction of $CO_2(aq)$ at the producer stabilizes at 0.82 after producing for 3.17*y*. As Equation (25) indicates the generation of carbonic acid through dissolution, the pH of brine in the aquifer decreases from the initial 7.2 to 4.7 at the injector (Fig. 6c) and continues to reduce with the expansion of the CO_2 plume. The final pH value stabilizes in the range 4.5–5 (Fig. 6a), and increases gradually towards the distal regions of the caprock and bedrock zones due to the penetration of CO_2. The maximum gas saturation in the injector is ~0.3 at 10*y*.

4.2. Mineral dissolution – precipitation

The acidification of the formation brine through dissolution of CO_2 induces primarily the partial dissolution of calcite, which dissolves rapidly with the injection of CO_2 as,

$$CaCO_3(solid) + CO_2 + H_2O \rightarrow Ca^{2+} + 2HCO_3^-$$

The dissolution of calcite contributes to slightly buffer the pH of the brine, by consuming the H^+ in water. Fig. 7 shows the volume fraction change of calcite in fracture and matrix from 1*y* to 10*y*. Calcite in the aquifer zone dissolves rapidly in the first 3*y*. The pH value is stabilized after 5*y* with the continuous injection of CO_2 (Fig. 6c). Due to the high concentration of supercritical CO_2 near the injector, the calcite dissolution is suppressed due to the absence of water in the stage of 0–5 *y*, while the dissolution activity is active between the middle and the production well. The top of the caprock and base of the bedrock display less pronounced dissolution, given the invasion of aqueous CO_2. As the aqueous CO_2 is difficult to diffuse into low permeable caprocks, the calcite precipitation could even be identified in the caprocks, which could serve protection in the sealing of caprocks (Fig. 7d). Furthermore, the brine saturated with aqueous CO_2 also dissolves the calcite adjacent to the rightmost edge of the domain near the injector during the later stage ~5-10*y*. A cross-plot of volume fraction change of calcite and Ca^{2+} concentration indicates minor precipitation of calcite at 3500–3750 *m* over the period 1-10*y* (Fig. 8). The local conditions of increased Ca^{2+} concentration and prevailing pH allow the precipitation of calcite according to the following reaction:

$$Ca^{2+} + 2HCO_3^- \rightarrow CaCO_3 + CO_2 + H_2O$$

4.3. Oligoclase dissolution and smectite precipitation

Another major dissolution component is oligoclase. The volume fraction change of oligoclase between the wells is shown in Fig. 9b, indicating continuous dissolution. There is pronounced dissolution between 1*y* to 5*y*. Similar to the dissolution of calcite, the high concentration in the CO_2 plume also inhibits dissolution near the injector. The dissolution of oligoclase proceeds preferentially under low pH conditions as,

$$CaNa_4Al_6Si_{14}O_{40}(oligoclase) + 6H^+ + 19H_20 \leftrightarrow Ca^{2+} + 4Na^+ + 3Al_2Si_2O_5(OH)_4 + 8Si(OH)_4$$

Hence, the dissolution of oligoclase provides a source of Ca^{2+} and

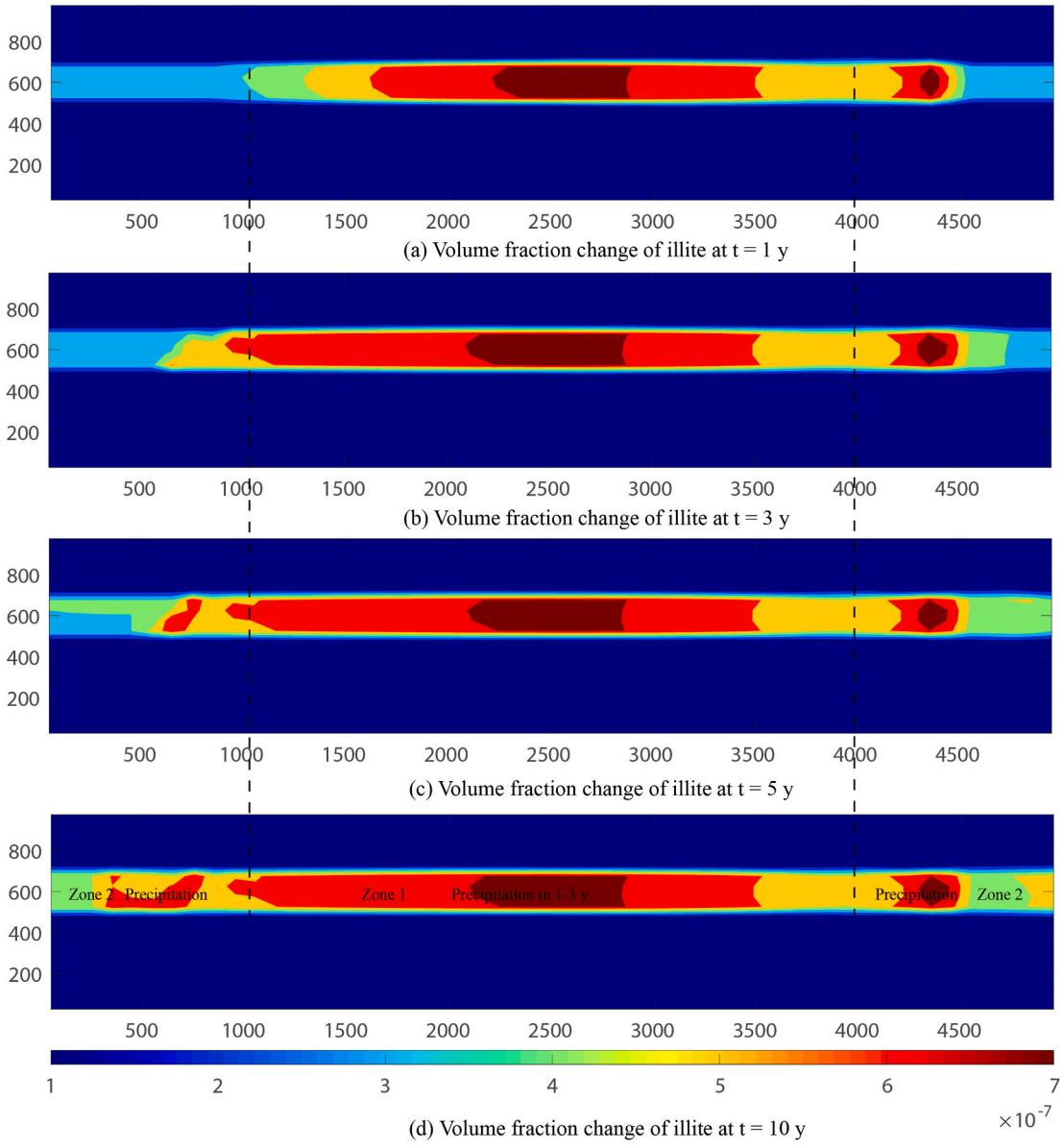

Fig. 14. Change in volume fraction of illite at (a) 1*y*, (b) 3*y*, (c) 5*y*, and (d) 10*y*.

Na^+, which later prompts the precipitation of smectite (Fig. 9a).

Fig. 9a depicts the distribution of the volume fraction change in smectite between the two wells. Precipitation of smectite terminates after 3*y*, which corresponds to the period for the major consumption of oligoclase (see Fig. 10). Similar observations are identified in the consumption of Mg^{2+} (Fig. 9c) and Na^+ (Fig. 9d). The precipitation of Na-smectite and Ca-smectite are described as,

$$0.26Mg^{2+} + 0.29Na^{+} + 1.77Al(OH)_3 + 3.97H_4SiO_4 \rightarrow Na_{0.29}Mg_{0.26}Al_{1.77}Si_{3.97}O_{10}(OH)_2 + 0.81H^{+} + 9.19H_2O \quad (Na-smectite)$$

$$0.26Mg^{2+} + 0.145Ca^{2+} + 1.77Al(OH)_3 + 3.97H_4SiO_4 \rightarrow Ca_{0.145}Mg_{0.26}Al_{1.77}Si_{3.97}O_{10}(OH)_2 + 0.81H^{+} + 9.19H_2O \quad (Ca-smectite)$$

The volume fraction change of smectite (Fig. 11) identifies that the majority of precipitation between injector and producer ceases after 3*y* as a secondary mineral, but some weak precipitation still continues

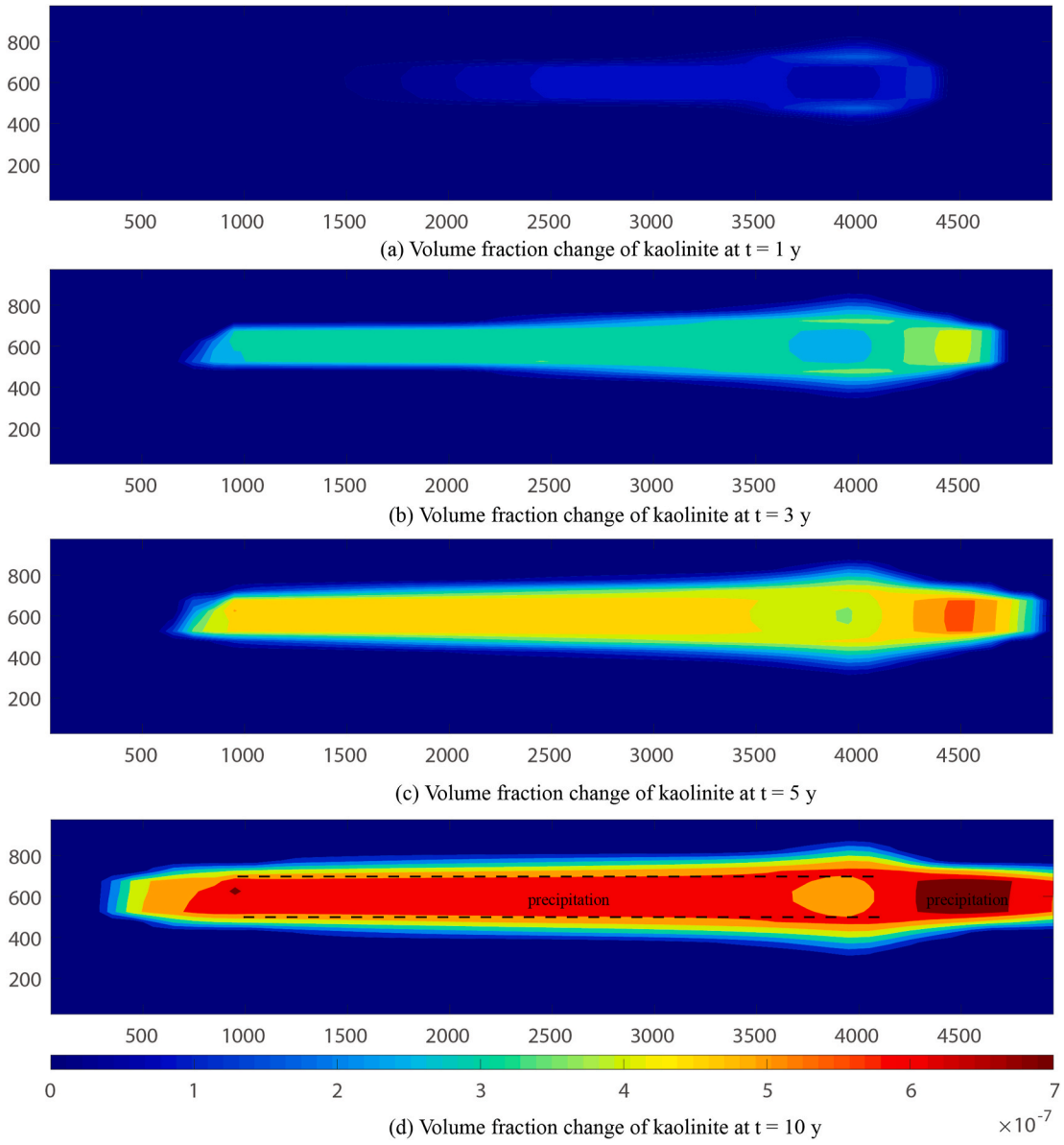

Fig. 15. Change in volume fraction change of kaolinite at (a) 1*y*, (b) 3*y*, (c) 5*y* and (d) 10*y*.

through later stages at the two edges of the aquifer zone (zone 2). The maximum fraction change of smectite precipitation is of the order of 10^{-6} and is not significant in modifying the porosity.

4.4. Feldspar dissolution and secondary mineral precipitation

Feldspar presents a kinetic reaction between dissolution and precipitation in the acidified brine.[20] The major dissolution process occurs by consuming H^+ and CO_2 and in converting into Al^{3+}, K^+, and illite precipitation following these reactions,

$$KAlSi_3O_9(K-feldspar) + 4H^+ = 2H_2O + Al^{3+} + K^+ + 3SiO_2(aq)$$

$$3KAlSi_3O_9(K-feldspar) + 2CO_2 + 2H_2O = KAl_2[AlSi_3O_{10}](OH)_2(illite) + 6SiO_2 + 2K^+ + 2HCO_3^-$$

The dissolved Al^{3+} also generates kaolinite precipitates. Fig. 12 presents the distribution of volume fraction change of feldspar at 1*y*, 3*y*, 5*y*, and 10*y*, respectively, and highlights the distinct separations between domains for dissolution and precipitation. We define three zones: zone 1 between the wells and within the aquifer, zone 2 as two wings at the edges of the aquifer, and zone 3 in the caprock and bedrock near the injector. Feldspar dissolution dominates in the caprock and bedrock (zone 3), providing a source of K^+ and Al^{3+} for the resulting precipitation of secondary minerals. The aquifer zone shows a cumulative precipitation of feldspar by increasing volume fraction by the 1*y* injection activity, while the dissolution of feldspar in the aquifer zone switched to be the major response. Synthesizing observations of the detailed concentration of K^+ (Fig. 13a) with the volume fraction change of feldspar (Fig. 13b) and illite (Fig. 13c), we postulate that both dissolution and precipitation occur in zone 1 and that the K^+ is consumed until 3*y* due to the initial high concentration and low pH condition before being converted into the precipitation of feldspar and illite in the aquifer layer. Zone 2 displays a slightly higher magnitude of feldspar precipitation, as a consequence of reduced dissolution.

The changes in volume fraction of illite from 1y to 10y are shown in Fig. 14. The pronounced precipitation of illite is identified in zone 2 as the two wings (zone 2) and zone 1 in the aquifer layer, while suppressed near injection well. This can be explained in that the dissolution of oligoclase also contributes to the precipitation in zone 2. The precipitation of illite primarily occurs in 0–3 *y*, which consistently overlaps with the reduction of K^+ concentration.

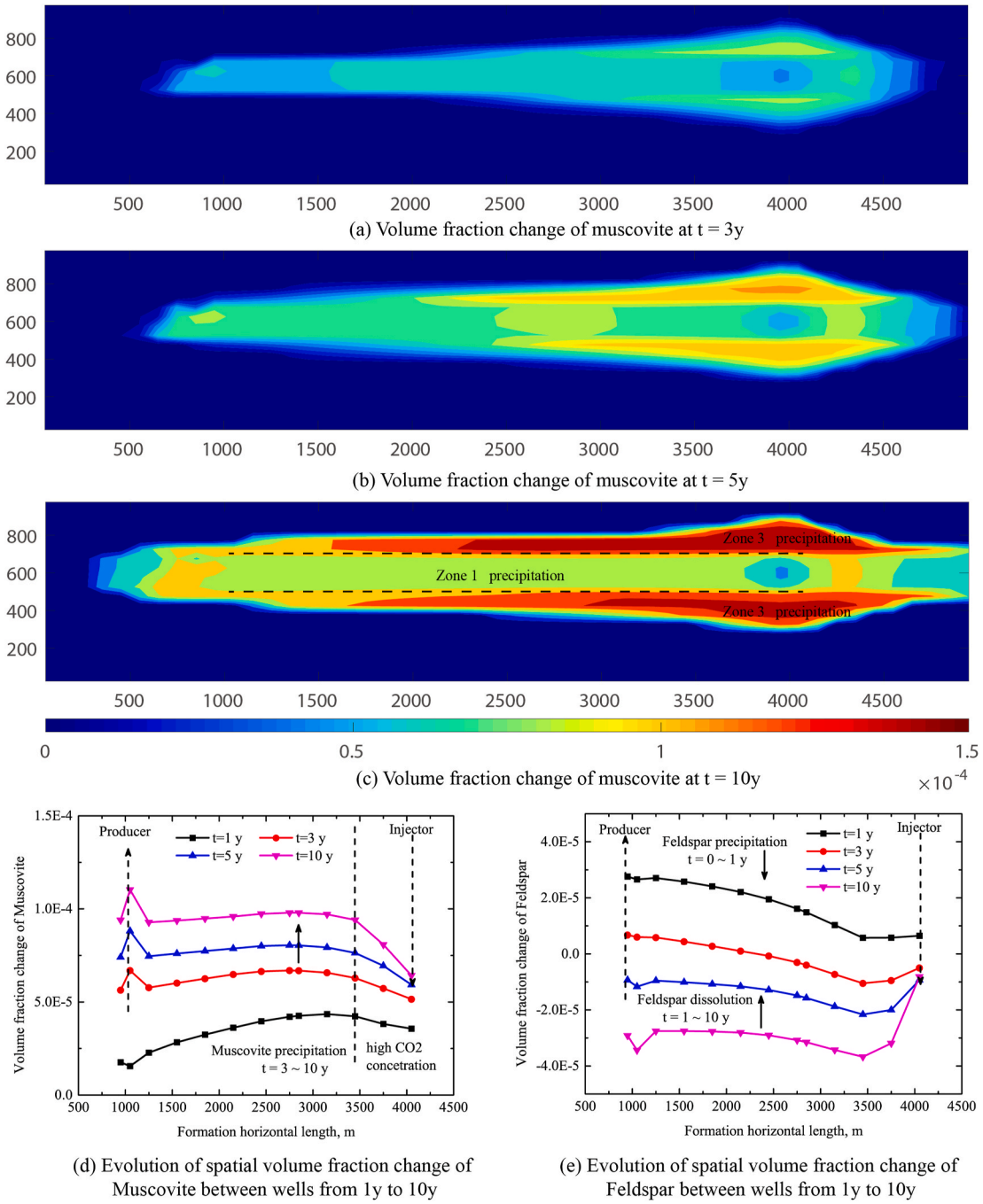

Fig. 16. Change in volume fraction of muscovite at (a) 3*y*, (b) *5y* and (c) 10*y* and the spatial distribution of change in volume fraction of (d) muscovite and (e) feldspar at 1y, 3*y*, *5y* and 10*y*.

Moreover, the distribution of the volume fraction change of feldspar between the wells reveals that dissolution of feldspar in aquifer zone 1 and caprock zone 3 occurs over 3-10*y* (Fig. 13 b-d), instead of continuous precipitation. The dissolution of feldspar and less reduction of K^+ over the 3-10*y* period facilitate the concurrent precipitation of kaolinite at this time (Fig. 13d). The precipitation of kaolinite will consume feldspar and Al^{3+} as,

$$2KAlSi_3O_8(K-feldspar) + 2H^+ + 9H_2O \rightarrow 2K^+ + Al_2Si_2O_5(OH)_4(kaolinite) + 4H_4SiO_4(aq)\,2Al^{3+} + 2SiO_2 + 5H_2O = Al_2Si_2O_5(OH)_4(kaolinite) + 6H^+$$

The evolution of volume fraction change of kaolinite is shown in Fig. 15 and illustrates the sequential process of kaolinite precipitation in the formation. Due to the initial dissolution of oligoclase and feldspar in zone 3 (caprock and bedrock), the kaolinite first precipitates in zone 3 until 5*y*. This potentially remediates the destruction of caprock integrity from the original dissolution of oligoclase and calcite. The precipitation of kaolinite is significantly enhanced in the aquifer zone (zone 1) during 5–10*y* (Fig. 15d), due to the consumption of K^+ and dissolution of feldspar (Fig. 13b). Consequently, the dissolution of feldspar is critical in determining the sequence of secondary mineral precipitation and locations. Kaolinite also precipitates in the caprock and bedrock to enhance the integrity of sealing.

Furthermore, the dissolution of feldspar also triggers precipitation of another secondary mineral, muscovite. Fig. 16 presents the volume fraction change of muscovite from 3*y* to 10*y*. Following a similar spatial pattern of precipitation to that of kaolinite, the muscovite also

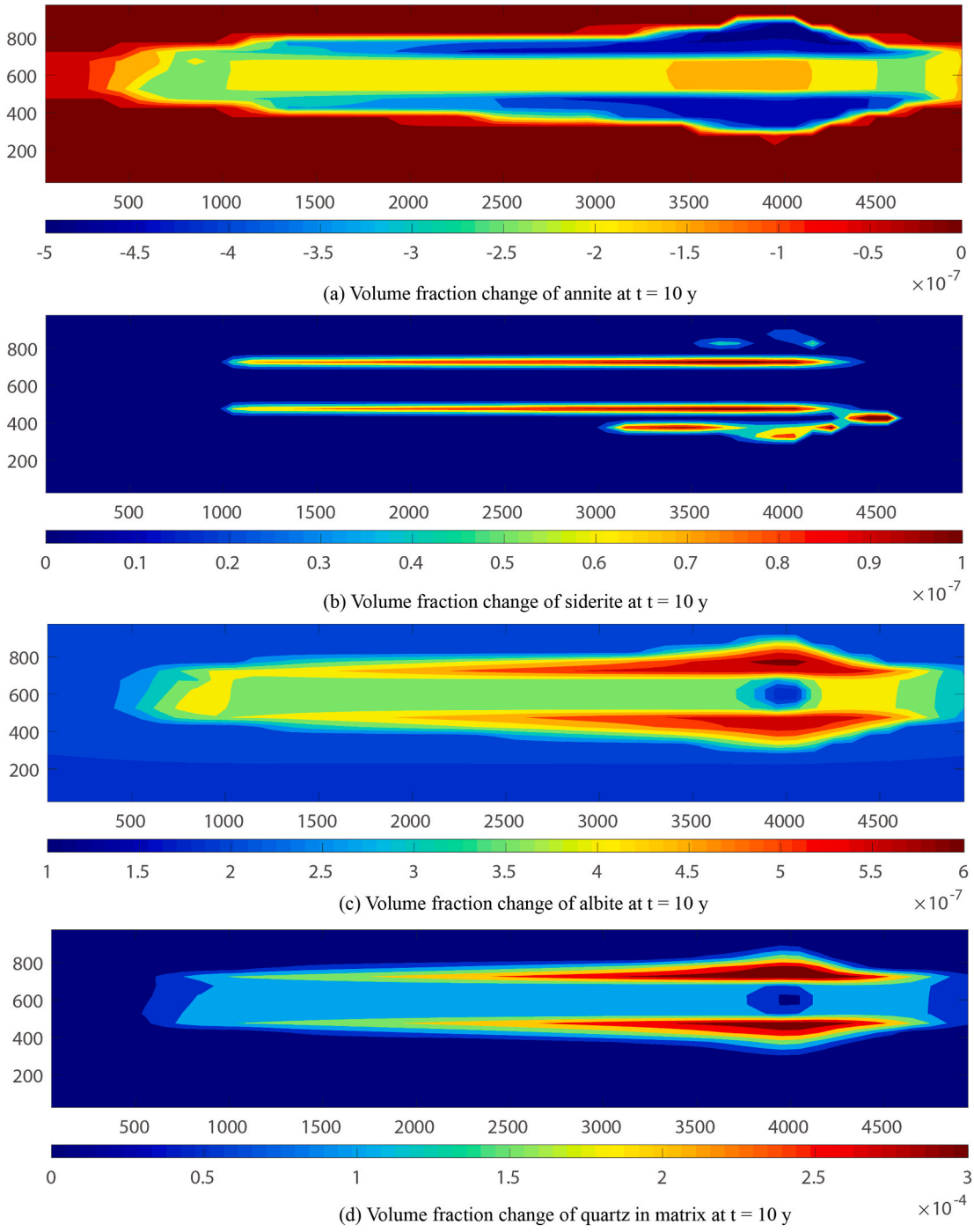

Fig. 17. Change in volume fraction of (a) annite, (b) siderite, (c) albite, and (d) quartz after 10*y*.

precipitates both in the caprock and the aquifer zone between wells.

$$KAlSi_3O_8(K-feldspar) + 4H_2O + 2Al^{3+} = KAl_3Si_3O_{10}(OH)_2(muscovite) + 6H^+$$

The volume fraction change in muscovite between the two wells is shown in Fig. 16c – precipitation in caprocks occurs principally from 3*y* to 10*y* and coincides with the timing of major feldspar dissolution in caprocks.

4.5. Secondary mineral dissolution and precipitation in caprock

The precipitation of secondary minerals primarily occurs in the caprock and bedrock and includes annite, muscovite, siderite, albite, and quartz. This precipitation of the secondary minerals acts to ensure the integrity of the caprock and bedrock, and prevents the working fluid

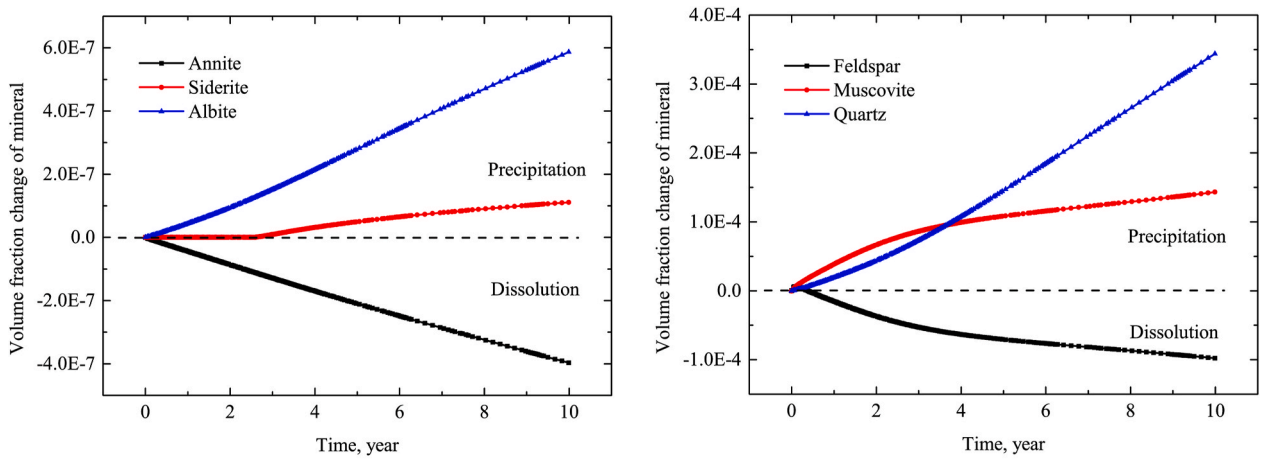

(a) Evolution of volume fraction change for the minerals Annite, Siderite, and Albite at caprock from initial to 10y.

(a) Evolution of volume fraction change for the minerals Feldspar, Muscovite, and Quartz at caprock from initial to 10y.

Fig. 18. Evolution of (a) change in volume fraction for annite, siderite and albite in caprock, and (b) volume fraction change for feldspar, muscovite, and quartz in the caprock.

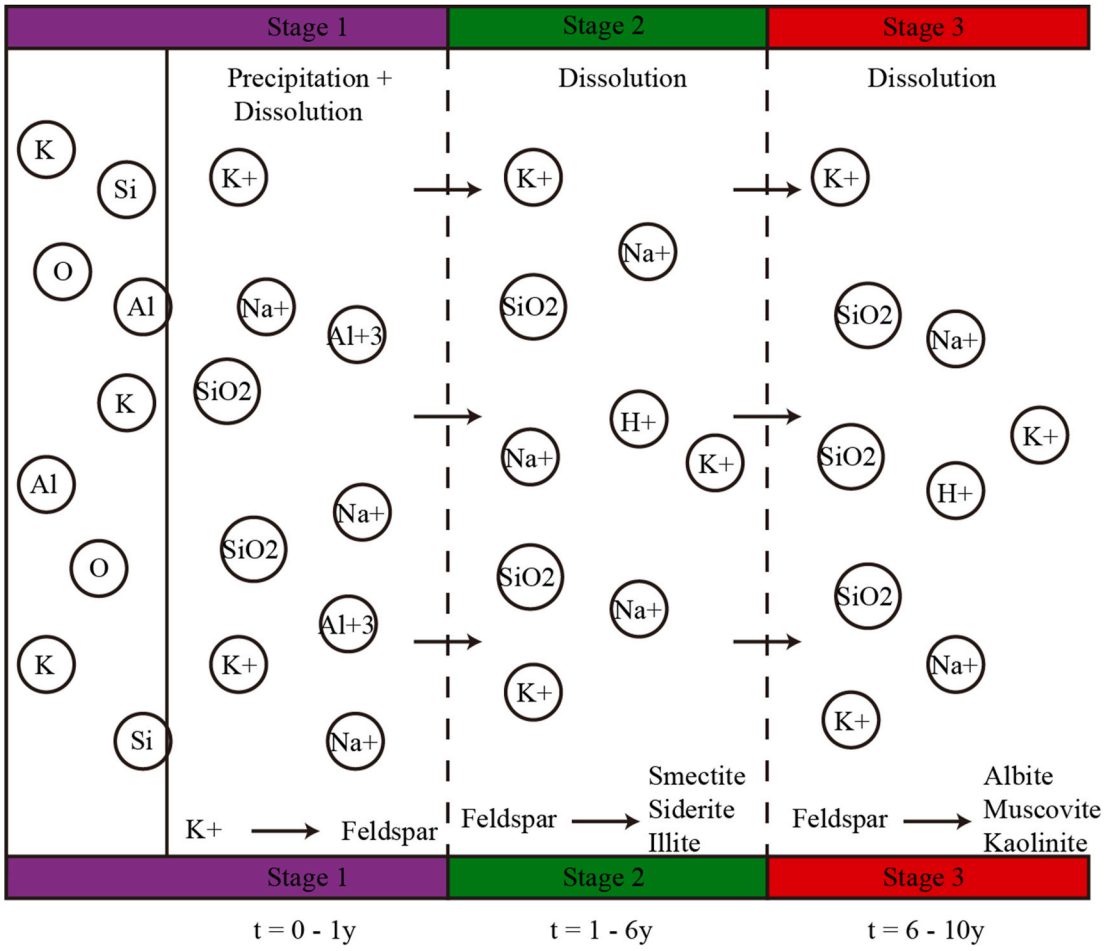

Fig. 19. Conceptual diagram to illustrate the proposed three stages dissolution – precipitation mechanism for feldspar.

Table 5
Five scenarios of fully-coupled (quadruplets) and partially-decoupled (triplets and one pair) models for the circulation of the two working fluids.

Scenario	Coupling physics	Working fluid	Injection enthalpy, J/kg	Injection rate, kg/s
Base Case 1	T-H-M-C	CO_2	2.8×10^5	1
2	H-M-C	CO_2	–	1
3	H-M	CO_2	–	1
4	T-H-C	CO_2	2.8×10^5	1
5	T-H-M	H_2O	1.57×10^5	1
6	T-H-M	CO_2	2.8×10^5	1

from further leak off. Fig. 17 shows the final distribution of volume fraction change of the four secondary minerals at 10*y*. The dissolution of the initial annite, feldspar, and oligoclase provides a source for the formation of muscovite, siderite, and quartz. The major dissolution of annite occurs in zone 3 (caprock and bedrock).

$$3KFe_3AlSi_3O_{10}(OH)_2(annite) + 11CO2 \rightarrow KAl_3Si_3O_{10}(OH)_2(muscovite) + 9FeCO_3(siderite) + 6SiO_2(quartz) + H_2O + 2K^+ + 2HCO3^- KAlSi_3O_8(feldspar) + Na^+ \rightarrow NaAlSi_3O_8(Albite) + K^+ KAlSi_3O_8(feldspar) + 4H^+ \rightarrow K^+ + Al^{3+} + 3SiO_2(quartz) + 2H_2O$$

The above chemical reactions demonstrate the conversion of secondary mineral precipitates through the dissolution of annite and feldspar. These secondary minerals predominantly precipitate in the caprock and bedrock near the injector, and further extend towards the producer. The volume fraction changes of annite, siderite and albite are

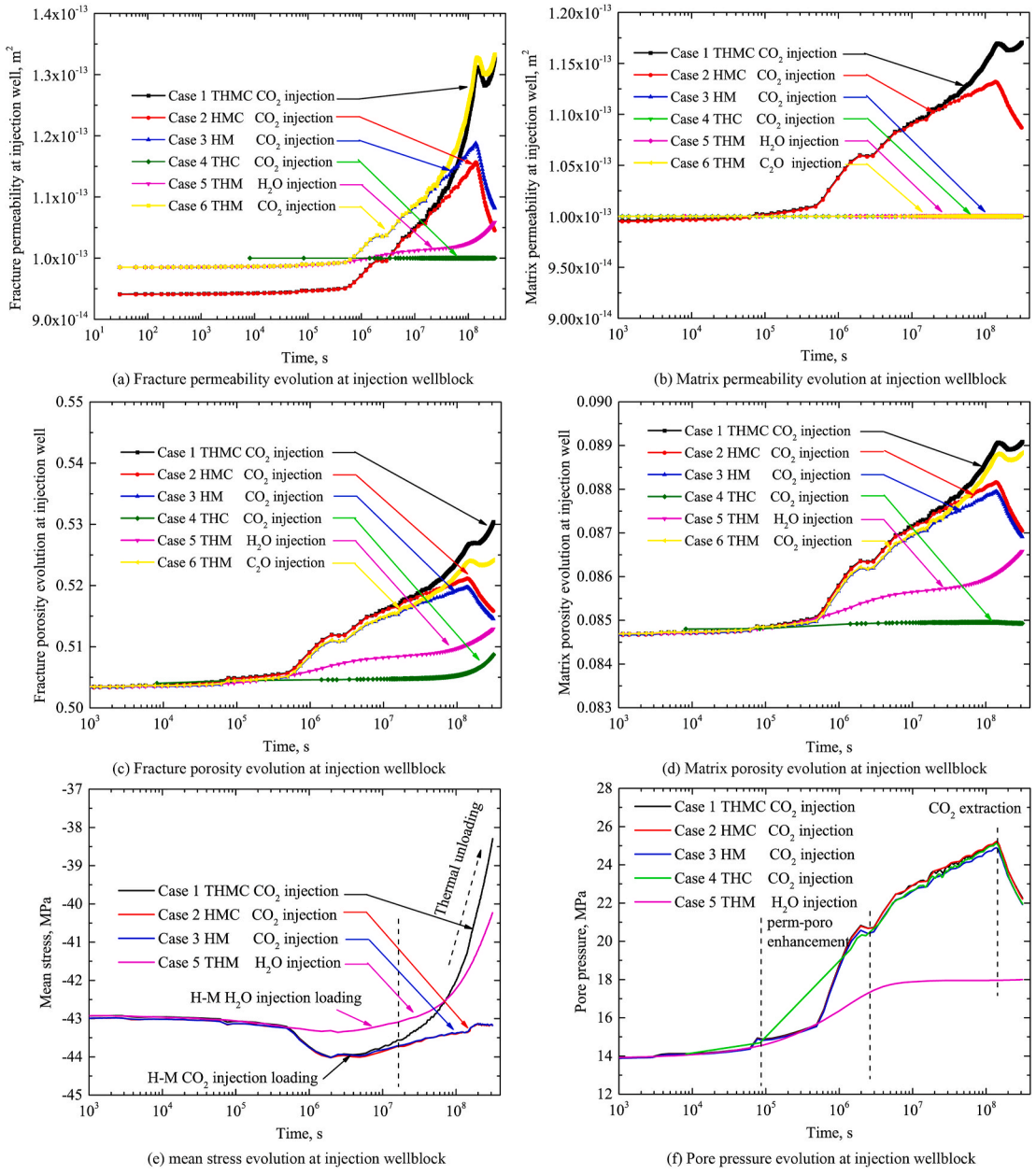

Fig. 20. Normalized evolution of (a) fracture permeability, (b) matrix permeability, (c) fracture porosity, and (d) matrix porosity at injection well-block for (Case 1) the fully coupled THMC-CO_2, (Case 2) the decoupled HMC-CO_2 case, (Case 3) the HMC-CO_2 case, (Case 4) the HM-CO_2 case, and (Case 5) the THM-H_20, and evolution of mean stress (e) and pore pressure (f) at injection well-block.

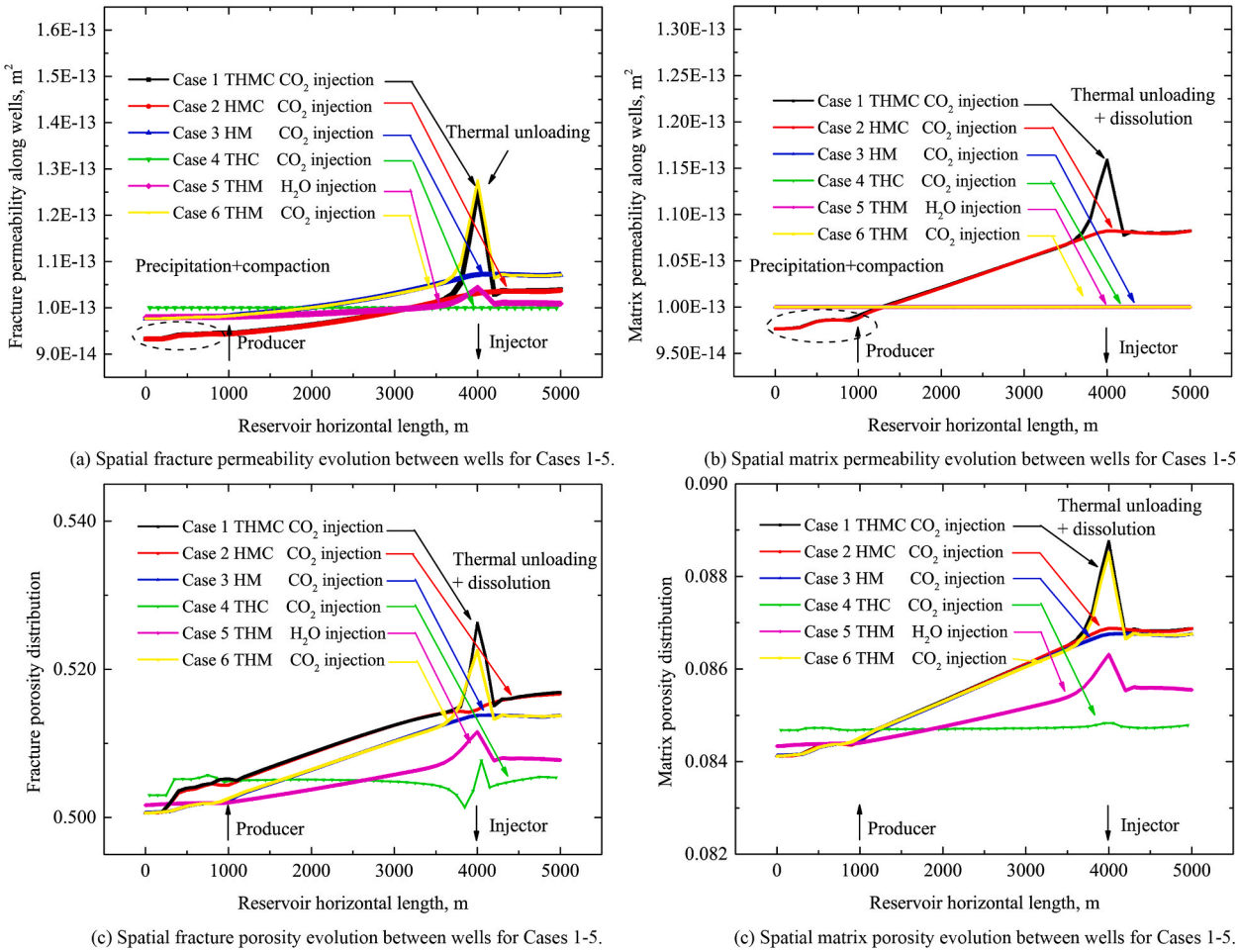

(a) Spatial fracture permeability evolution between wells for Cases 1-5.

(b) Spatial matrix permeability evolution between wells for Cases 1-5.

(c) Spatial fracture porosity evolution between wells for Cases 1-5.

(c) Spatial matrix porosity evolution between wells for Cases 1-5.

Fig. 21. Spatial distribution of (a) fracture permeability and (c) porosity, and matrix (b) permeability, and (d) porosity between injection well and production well at different simulation scenarios (Case 1–6).

of the order of 10^{-7} after 10*y*. The high concentration of the $scCO_2$ plume near the injector zones also inhibits the precipitation of secondary minerals. This may be beneficial in preventing scaling in the wellbore. Examining the distribution of quartz indicates that the majority of the quartz is deposited in caprock and bedrom (zone 3) as precipitation to reduce the porosity to a fraction of 3×10^{-4}, while the circulation path within the aquifer has a relatively smaller mass of quartz precipitation as it would destroy or plug the permeable channel significantly.[28] The detailed consumption and generation of secondary minerals in the caprock is shown in Fig. 18. Clearly, the siderite only begins to precipitate after 3*y*, due to the dissolution of feldspar. The precipitations of muscovite and quartz are also strongly associated with the dissolution of feldspar (Fig. 18b).

The preceding has clearly identified the relationship between feldspar dissolution–precipitation order and the associated precipitation of secondary minerals in zone 3 (caprock and bedrock). We propose a three-stage conceptual model for feldspar dissolution and timing (Fig. 19), building from short-term (100h) experimental observations of feldspar dissolution.[20] Based on the initial setting and corresponding observations, we hypothesize that the precipitation of feldspar dominates at early time (0-1*y*) due to the high concentration of K^+. The feldspar tends to be dissolved after the increasing fraction from the first stage, and precipitates siderite, smectite and illite in a second stage at ~1 - 6*y*. The final and third stage represents the major precipitation of albite, muscovite, and kaolinite at ~6 - 10*y*, by dissolving the feldspar in the aquifer and caprocks. This sequentially staged model may also be applied to address the spatial distribution of secondary minerals.

4.6. Evolution of permeability and porosity

Dissolution and precipitation of primary and secondary minerals exert a significant impact in the evolution of permeability and porosity for both fractures and matrix especially near injection well. Constitutive models governing the evolution of permeability and porosity are detailed in Equations 14–23. It is critical to examine the complex competition among each individual component in modifying the properties of the aquifer and caprocks. Therefore, six parametric simulations are designated in Table 5 to represent different six coupled and injection model scenarios to define the implications of porosity and permeability evolution. The base case (Case 1) represents the fully coupled T-H-M-C model; Case 2 decouples thermal influence and represents only H-M-C coupling; Case 6 decouples chemical influence with only T-H-M coupling; Case 3 represents only H-M coupling; and Case 4 runs only TOUGH-ECO2N in decoupled mode without mechanical interactions (T-H-C coupling, only). Cases 1–4 and 6 all implement CO_2 as the working fluid. In contrast, Case 5 circulates conventional H_2O under 1 kg/s and same temperature with CO_2 as the working fluid and applies a T-H-M coupled model. The intention of these scenarios is to evaluate the thermal depletion efficiency with different working fluids, and to assess the critical components of coupling that influence heat transfer (T), mechanical deformation (M), and chemical reaction (C) feedbacks in controlling the evolution of fracture & matrix permeability and porosity across a range of spatial and temporal scales.

Fig. 20 presents the history of permeability and porosity evolution for both fracture and matrix in the injection well-block. The initial

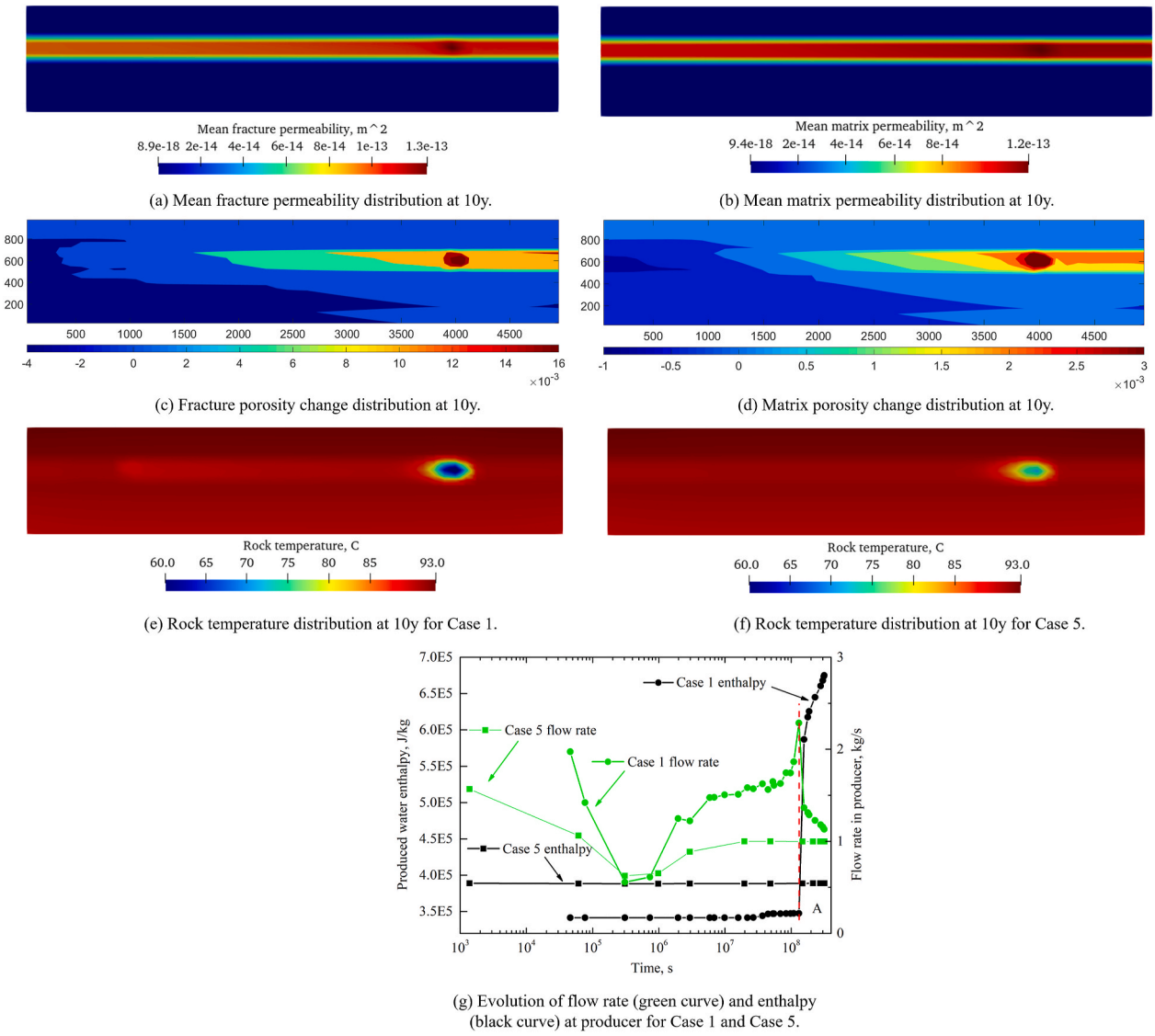

(a) Mean fracture permeability distribution at 10y.

(b) Mean matrix permeability distribution at 10y.

(c) Fracture porosity change distribution at 10y.

(d) Matrix porosity change distribution at 10y.

(e) Rock temperature distribution at 10y for Case 1.

(f) Rock temperature distribution at 10y for Case 5.

(g) Evolution of flow rate (green curve) and enthalpy (black curve) at producer for Case 1 and Case 5.

Fig. 22. Distribution of (a) mean fracture permeability and (b) mean matrix permeability at 10y for Case 1, rock temperature distribution at 10y for Case 1 (c) and Case 5 (d), and evolution of flow rate (green curve) and enthalpy (black curve) at producer for Case 1 and Case 5 (e) separately. (For interpretation of the references to colour in this figure legend, the reader is referred to the Web version of this article.)

mineral components defined in fractures could slightly reduce the initial magnitude of permeability (9.85×10^{-14} m^2). The fracture permeability indicates that the highest permeability growth range occurs for the fully coupled Case 1 (THMC-CO_2) where permeability is enhanced 1.4 times relative to the initial permeability. This compares against the 1.23 times enhancement for Case 2 (HMC-CO_2), and 1.20 times enhancement for Case 3 (HM-CO_2). In this, the strong thermal cooling has a significant impact in enhancing the fracture aperture near injector. Without engaging the separate constitutive models for the fracture aperture evolution, Case 4 (THC-CO_2) with rigid and non-deforming fractures presents no significant changes in the permeability. Furthermore, it reveals that CO_2 injection significantly enhances the permeability, compared against using the water as working fluid (Case 5). Similarly, the matrix permeability is enhanced by 1.18 times in Case 1. The stress change resulting from thermal unloading also contributes nearly 90% in the final enhancement of matrix permeability.

Fig. 20e presents the evolution of mean stress in the same injection well-block for Cases 1–5. Even though the injected water and CO_2 share the identical injection rates and temperature, the injection of CO_2 significantly reduces the mean stress around 5 MPa, as driven by the thermal unloading response.[48,49] The CO_2 expansion due to phase transition after injecting into the reservoir causes stressing response by enhancing the local stress state from 5×10^5 *s*. Due to the growth of permeability and porosity around injection well, the pore pressure increasing gradient in the Case 1–3 remains smaller than the pressure growth gradient in the Case 4. The water injection in Case 5 requires less pressure power to maintain the injection rate of 1 kg/s. The pressure reduction from 1.2×10^8 s suggests the reduction of gas partial pressure in the reservoir, by extracting gas phase saturated in the reservoir brine. The response of pressure reduction brings a slight reduction in the permeability and porosity.

Comparison of fracture and matrix porosity for the six cases suggests that the fully coupled Case 1 produces the highest porosity enhancement for both fracture and matrix ~1.06 times. Mechanical unloading due to direct pressurization and thermal drawdown in Case 1 enhances the porosity at the early then later stages, respectively, compared to the rigid and non-deforming model of Case 4. Dissolution exerts a slightly larger influence in enhancing fracture porosity (~0.01) relative to observed changes in matrix porosity (~0.001).

Fig. 21 examines the spatial distribution of permeability along a line connecting the wells for the same 6 Cases at the end of 10*y*, and the comparison of flow rate and associated enthalpy in the production well

between Case 1 and Case 6. Fracture and matrix permeability within a radius of 1000 *m* from the injector are enhanced relative to the initial magnitude, while the permeability at the producer is reduced due to the influence of precipitation and compaction. The thermal unloading response also partially remediates the influence of precipitation by enhancing fracture permeability and porosity near the injector, as shown by the significant peak displayed for Case 1 representing the fully coupled T-H-M-C model (Fig. 21a, c). The injection of CO_2 substantially enhances the permeability and porosity throughout the entire aquifer. Dissolution enhanced the fracture porosity around ~0.002 in the aquifer within 10*y*, while the influence of dissolution in augmenting matrix porosity is limited. The spatial distribution of permeability and porosity suggests that thermal unloading and dissolution are the two principal mechanisms enhancing permeability and porosity of fractures within the aquifer.

Fig. 22(a–d) illustrates the distributions of permeability and porosity change in fracture and matrix at 10*y* for Case 1, identifying the enhancement or destruction of fracture and matrix properties (permeability and porosity). The porosity of fracture and matrix around injection well are enhanced at 0.016 and 0.003 separately, while the precipitation & production leads to porosity reduction in the left side of aquifer layer. Furthermore, the rock temperature distributions (e, f) at 10*y* for Case 1 (THMC-CO_2) and Case 5 (THM-H_2O) are provided to highlight the efficiency of heat extraction for the different working fluids – CO_2 and H_2O. The injection rate and temperature of fluids are retained identical to allow direct comparison. Apparently, the $scCO_2$ injection of Case 1 achieves a higher efficiency in heat recovery. This is apparent in that the aquifer is cooler for recovery by CO_2 relative to that for H_2O. Consequently, the results suggest that $scCO_2$ could be implemented as an effective working fluid in enhancing heat extraction efficiency, while also preventing significant scaling issues that reduces wellbore connectivity over the long term. The heat energy extraction efficiency could also be highlighted by comparing the flow rate and corresponded enthalpy of produced fluid. Fig. 22g compares the evolution of fluid flow rate and enthalpy for Case 1 and 5 within 10*y*. The produced flow rate and enthalpy for water working fluid are kept at 1 kg/s and 4.5×10^5 J/kg, while the CO_2 circulation could enhance the flow rate up to 2.5 kg/s, and the enthalpy of produced fluid could be increased up to 6.5×10^5 J/kg due to the increasing concentration of $scCO_2$ in production well after 1.2×10^8 *s*. Thereby it could substantially enhance the energy recovery efficiency.

5. Conclusions

A fully coupled THMC model has been developed to address the feasibility of using $scCO_2$ as a working fluid in geothermal reservoirs. After continuously injecting supercritical CO_2 (35 °C) into a permeable aquifer, bounded by impermeable caprock and bedrock layers, the formation pH magnitude is reduced from 7 to 4.5 due to rapid dissolution of CO_2 and calcite. The injected CO_2 are sequestrated by solubility trapping in water, and reaches a maximum capacity of $\sim 2 \times 10^7$ kg at $t = 2 \times 10^8$s (6.34*y*). The mass concentration in the production well start to increase. As the CO_2 plume near the injector inhibits chemical reactions under anhydrous conditions, calcite is dissolved with the propagation of aqueous CO_2 in the aquifer zone and the caprock zones above the injector. The increasing concentration of Ca^{2+} triggers calcite precipitation away from injector in late time ~10*y*. The dissolution of oligoclase provides a source of Na+ and Mg^{2+}, which facilitates the precipitation of the secondary minerals Na-smectite and Ca-smectite in the aquifer zone.

A conceptual three-stage sequential model is used to illustrate the kinetic process of feldspar dissolution and precipitation at different times. The initial high concentration of K^+ allows the feldspar to precipitate firstly by consuming K^+ until 5*y*. The feldspar begins to dissolve and converts into precipitates of illite, siderite, and muscovite in the aquifer zone at 1-6*y* in the second stage. The secondary minerals of albite, muscovite, and kaolinite mostly precipitate in the aquifer layer in the last stage at 6-10*y*. The dissolution of oligoclase and feldspar in the caprock and bedrock provide ions of Na^+, K^+, and Ca^{2+} to develop precipitates of siderite, quartz and albite in the caprock and bedrock, which maintains the integrity of caprock seal.

Volume expansion of CO_2 resulting from its phase transition provides a stronger source than conventional water circulation in pressurizing formation. Fracture permeability and porosity in the aquifer zone are enhanced at around 1.4 and 1.2 times over its initial magnitude after 10 years of injection-production, especially near the injector due to the strong influence of thermal unloading. The thermal unloading is more pronounced than chemical dissolution in improving formation permeability, although secondary precipitation may be identified in reducing permeability and porosity near the injector and edge boundaries. The linkage between porosity growth resulting from dissolution and modulus & strength reduction is not accounted, due to lack of the reliable constitutive model or experiment data, which could accurately replicate the cementation collapse in reducing strength of rocks. This response could be explored in the future work. The chemical dissolution in enhancing permeability and porosity near the injection well takes place from 10^8*s (*1157*d)*. Spatial profiles of permeability and porosity evolution in the aquifer layer suggest that the permeability and porosity will be more greatly enhanced with $scCO_2$ injection, compared with the marginal enhancement due to water-based circulation.

Furthermore, the $scCO_2$ circulation has an advantage in extracting more heat energy from the host rock, which could make up for the reduced flow rate resulting potential leak off. The concentration of scCO2 in production well reaches the peak magnitude of 0.82 after 1.2×10^8*s*, which could result in the enhancement of fluid enthalpy up to 6.5×10^5 J/kg, due to the high heat capacity of $scCO_2$. The improved formation permeability also facilitates a larger mass flow rate at 2 kg/s in the production well, comparing to the 1 kg/s in the conventional water circulation scenario. Consequently, we can conclude that supercritical CO_2 could be implemented as an effective circulating fluid in geothermal energy extraction, and avoiding the potential damage due to wellbore scaling.

Declaration of competing interest

The authors declare that they have no known competing financial interests or personal relationships that could have appeared to influence the work reported in this paper.

Acknowledgement

This project was partly subsidized through the ERANET Cofund GEOTHERMICA (Project no. 731117), from the European Commission, Topsector Energy subsidy from the Ministry of Economic Affairs of the Netherlands, Federal Ministry for Economic Affairs and Energy of Germany and EUDP, and the Science and Technology Department of Sichuan Province (Grant No. 21YFH0048).

References

1 Gan Q, Elsworth D, Alpern JS, Marone C, Connolly P. Breakdown pressures due to infiltration and exclusion in finite length boreholes. *J Petrol Sci Eng.* 2015;127:329–337.
2 Jia Y, Lu Y, Elsworth D, Fang Y, Tang J. Surface characteristics and permeability enhancement of shale fractures due to water and supercritical carbon dioxide fracturing. *J Petrol Sci Eng.* 2018;165:284–297.
3 Sampath KHSM, Perera MSA, Ranj, , et alTao X. CH4CO2 gas exchange and supercritical CO2 based hydraulic fracturing as CBM production-accelerating techniques: a review. *J. CO2 Utilization.* 2017;22:212–230.
4 Mukherjee M, Misra S. A review of experimental research on Enhanced Coal Bed Methane (ECBM) recovery via CO_2 sequestration. *Earth Sci Rev.* 2018;179:392–410.
5 Brown DW. January. A hot dry rock geothermal energy concept utilizing supercritical CO2 instead of water. In: *Proceedings of the Twenty-Fifth Workshop on Geothermal Reservoir Engineering.* Stanford University; 2000:233–238.

6 Pruess K. Enhanced geothermal systems (EGS) using CO2 as working fluid—a novel approach for generating renewable energy with simultaneous sequestration of carbon. *Geothermics*. 2006;35(4):351–367.
7 Fouillac C, Sanjuan B, Gentier S, Czernichowski-Lauriol I. May. Could sequestration of CO2 be combined with the development of enhanced geothermal systems. In: *Third Annual Conference on Carbon Capture and Sequestration, Alexandria, VA*. vol. 4. 2004.
8 Xu T, Pruess K. April. Reactive transport modeling to study fluid-rock interactions in enhanced geothermal systems (EGS) with CO2 as working fluid. In: *Proceedings, World Geothermal Congress*. vol. 20. 2010.
9 Zhang R, Yin X, Winterfeld PH, Wu YS. A fully coupled thermal-hydrological-mechanical-chemical model for CO2 geological sequestration. *J Nat Gas Sci Eng*. 2016;28:280–304.
10 Zhang R, Wu YS. Hydrologic, mechanical, thermal, and chemical process coupling triggered by the injection of CO2. In: *Science of Carbon Storage in Deep Saline Formations*. Elsevier; 2019:361–381.
11 Xu T, Apps JA, Pruess K. Reactive geochemical transport simulation to study mineral trapping for CO2 disposal in deep arenaceous formations. *J Geophys Res: Solid Earth*. 2003;108(B2).
12 Szulczewski ML, MacMinn CW, Herzog HJ, Juanes R. Lifetime of carbon capture and storage as a climate-change mitigation technology. *Proc Natl Acad Sci Unit States Am*. 2012;109(14):5185–5189.
13 Ueda A, Kato K, O, , et alakase H. Experimental studies of CO2-rock interaction at elevated temperatures under hydrothermal conditions. *Geochem J*. 2005;39(5):417–425.
14 André L, Audigane P, Azaroual M, Menjoz A. Numerical modeling of fluid–rock chemical interactions at the supercritical CO2–liquid interface during CO2 injection into a carbonate reservoir, the Dogger aquifer (Paris Basin, France). *Energy Convers Manag*. 2007;48(6):1782–1797.
15 Pimienta L, Esteban L, S, , et alell MB. Supercritical CO_2 injection and residence time in fluid-saturated rocks: evidence for calcite dissolution and effects on rock integrity. *Int. J. Greenhouse Gas Control*. 2017;67:31–48.
16 Gan Q, Elsworth D. Analysis of fluid injection-induced fault reactivation and seismic slip in geothermal reservoirs. *J Geophys Res: Solid Earth*. 2014;119(4):3340–3353.
17 Gan Q, Elsworth D. Thermal drawdown and late-stage seismic-slip fault reactivation in enhanced geothermal reservoirs. *J Geophys Res: Solid Earth*. 2014;119(12):8936–8949.
18 Cappa F, Rutqvist J. Modeling of coupled deformation and permeability evolution during fault reactivation induced by deep underground injection of CO2. *Int. J. Greenhouse Gas Control*. 2011;5(2):336–346.
19 Peng C, Crawshaw JP, Maitland GC, Trusler JM. Kinetics of calcite dissolution in CO2-saturated water at temperatures between (323 and 373) K and pressures up to 13.8 MPa. *Chem Geol*. 2015;403:74–85.
20 Li M, Li C, Xing J, Sun X, Yuan G, Cao Y. An experimental study on dynamic coupling process of alkaline feldspar dissolution and secondary mineral precipitation. *Acta Geochimica*. 2019;38(6):872–882.
21 Burton EA, Walter LM. Relative precipitation rates of aragonite and Mg calcite from seawater: temperature or carbonate ion control? *Geology*. 1987;15(2):111–114.
22 Krauskopf KB. Dissolution and precipitation of silica at low temperatures. *Geochem Cosmochim Acta*. 1956;10(1-2):1–26.
23 Faoro I, Elsworth D, Candela T. Evolution of the transport properties of fractures subject to thermally and mechanically activated mineral alteration and redistribution. *Geofluids*. 2016;16(3):396–407.
24 Lu P, Fu Q, Seyfried, , et alZhu C. Coupled alkali feldspar dissolution and secondary mineral precipitation in batch systems–2: new experiments with supercritical CO2 and implications for carbon sequestration. *Appl Geochem*. 2013;30:75–90.
25 Barton N, Bandis S, Bakhtar K. June. Strength, deformation and conductivity coupling of rock joints. In: *International Journal of Rock Mechanics and Mining Sciences & Geomechanics Abstracts*. vol. 22. Pergamon; 1985:121–140. , No. 3.
26 Gan Q, Elsworth D. A continuum model for coupled stress and fluid flow in discrete fracture networks. *Geomechanics and Geophysics for Geo-Energy and Geo-Resources*. 2016;2(1):43–61.
27 Baghbanan A, Jing L. Hydraulic properties of fractured rock masses with correlated fracture length and aperture. *Int J Rock Mech Min Sci*. 2007;44(5):704–719.
28 Taron J, Elsworth D. Coupled mechanical and chemical processes in engineered geothermal reservoirs with dynamic permeability. *Int J Rock Mech Min Sci*. 2010;47(8):1339–1348.
29 Yasuhara H, Marone C, Elsworth D. Fault zone restrengthening and frictional healing: the role of pressure solution. *J Geophys Res: Solid Earth*. 2005;110(B6).
30 Tada R, Siever R. Pressure solution during diagenesis. *Annu Rev Earth Planet Sci*. 1989;17:89.
31 Pruess K. *ECO2N: A TOUGH2 Fluid Property Module for Mixtures of Water, NaCl, and CO2*. Berkeley, CA: Lawrence Berkeley National Laboratory; 2005:76.
32 Taron J, Elsworth D, Min KB. Numerical simulation of thermal-hydrologic-mechanical-chemical processes in deformable, fractured porous media. *Int J Rock Mech Min Sci*. 2009;46(5):842–854.
33 Wilson RK, Aifantis EC. On the theory of consolidation with double porosity. *Int J Eng Sci*. 1982;20(9):1009–1035.
34 Lasaga AC. Chemical kinetics of water-rock interactions. *J Geophys Res: solid earth*. 1984;89(B6):4009–4025.
35 Steefel CI, Lasaga AC. A coupled model for transport of multiple chemical species and kinetic precipitation/dissolution reactions with application to reactive flow in single phase hydrothermal systems. *Am J Sci*. 1994;294(5):529–592.
36 Davies JP, Davies DK. January. Stress-dependent permeability: characterization and modeling. In: *SPE Annual Technical Conference and Exhibition*. Society of Petroleum Engineers; 1999.
37 Rutqvist J, Wu YS, Tsang CF, Bodvarsson G. A modeling approach for analysis of coupled multiphase fluid flow, heat transfer, and deformation in fractured porous rock. *Int J Rock Mech Min Sci*. 2002;39(4):429–442.
38 Lichtner PC. Continuum formulation of multicomponent-multiphase reactive transport. *Rev Mineral*. 1996;34:1–82.
39 Snow DT. Anisotropie permeability of fractured media. *Water Resour Res*. 1969;5(6):1273–1289.
40 Bear J. *Dynamics of Fluids in Porous Media*. Courier Corporation; 2013.
41 Rauzi SL. *Carbon Dioxide in the St*. Apache County, Arizona: Johns-Springerville Area; 1999.
42 Leverett M. Capillary behavior in porous solids. *Transactions of the AIME*. 1941;142:152–169, 01.
43 Udell KS, Fitch JS. August. Heat and mass transfer in capillary porous media considering evaporation, condensation, and non-condensible gas effects. In: *23rd ASME/AIChE National Heat Transfer Conference, Denver, CO*. 1985:103–110.
44 Audigane P, Gaus I, Czernichowski-Lauriol I, Pruess K, Xu T. Two-dimensional reactive transport modeling of CO2 injection in a saline aquifer at the Sleipner site, North Sea. *Am J Sci*. 2007;307(7):974–1008.
45 Corey AT. The interrelation between gas and oil relative permeabilities. *Prod Mon*. 1954;19(1):38–41.
46 Pan F, McPherson BJ, Kaszuba J. *Evaluation of CO2-fluid-rock Interaction in Enhanced Geothermal Systems: Field-Scale Geochemical Simulations*. Geofluids; 2017:2017.
47 Xu T, Spycher N, Sonnenthal E, Zhang G, Zheng L, Pruess K. TOUGHREACT Version 2.0: a simulator for subsurface reactive transport under non-isothermal multiphase flow conditions. *Comput Geosci*. 2011;37(6):763–774.
48 Gan Q, Lei Q. Induced fault reactivation by thermal perturbation in enhanced geothermal systems. *Geothermics*. 2020;86:101814.
49 Gan Q, Elsworth D. Production optimization in fractured geothermal reservoirs by coupled discrete fracture network modeling. *Geothermics*. 2016;62:131–142.